



Helium trapping in apatite damage: Insights from (U-Th-Sm)/He dating of different granitoid lithologies

Alice Recanati, Cécile Gautheron, Jocelyn Barbarand, Yves Missenard, Rosella Pinna-Jamme, Laurent Tassan-Got, Andy Carter, Éric Douville, Louise Bordier, Maurice Pagel, et al.

► To cite this version:

Alice Recanati, Cécile Gautheron, Jocelyn Barbarand, Yves Missenard, Rosella Pinna-Jamme, et al.. Helium trapping in apatite damage: Insights from (U-Th-Sm)/He dating of different granitoid lithologies. *Chemical Geology*, 2017, 470, pp.116-131. 10.1016/j.chemgeo.2017.09.002 . insu-01588347

HAL Id: insu-01588347

<https://insu.hal.science/insu-01588347>

Submitted on 5 Mar 2021

HAL is a multi-disciplinary open access archive for the deposit and dissemination of scientific research documents, whether they are published or not. The documents may come from teaching and research institutions in France or abroad, or from public or private research centers.

L'archive ouverte pluridisciplinaire **HAL**, est destinée au dépôt et à la diffusion de documents scientifiques de niveau recherche, publiés ou non, émanant des établissements d'enseignement et de recherche français ou étrangers, des laboratoires publics ou privés.

BIROn - Birkbeck Institutional Research Online

Recanati, A. and Gautheron, C. and Barbarand, J. and Missenard, Y. and Pinna-Jamme, R. and Tassan-Got, L. and Carter, Andrew and Douville, E. and Bordier, L. and Pagel, M. and Gallagher, K. (2017) Helium trapping in apatite damage: insights from (U-Th-Sm)/He dating of different granitoid lithologies. *Chemical Geology* 470 , pp. 116-131. ISSN 0009-2541.

Downloaded from: <http://eprints.bbk.ac.uk/id/eprint/20383/>

Usage Guidelines:

Please refer to usage guidelines at <https://eprints.bbk.ac.uk/policies.html>
contact lib-eprints@bbk.ac.uk.

or alternatively

Helium trapping in apatite damage: insights from (U-Th-Sm)/He dating of different granitoid lithologies

Alice Recanati^{1*}, Cécile Gautheron¹, Jocelyn Barbarand¹, Yves Missenard¹,
Rosella Pinna-Jamme¹, Laurent Tassan-Got², Andy Carter³, Eric Douville⁴,
Louise Bordier⁴, Maurice Pagel¹, Kerry Gallagher⁵

¹ GEOPS, Univ Paris Sud, CNRS, Université Paris-Saclay, Rue du Belvédère, Bât. 504,
Orsay, F-91405, France

² Institut de Physique Nucleaire, Université Paris Sud, CNRS/IN2P3, 91405 Orsay, France,

³ Dept. of Earth and Planetary Sciences, Birkbeck, University of London, UK

⁴ Laboratoire des Sciences du Climat et de l'Environnement (LSCE/IPSL), CEA- CNRS-
UVSQ, Université Paris-saclay, F-91191 Gif sur Yvette, France

⁵ Géosciences Rennes, Université Rennes 1, Rennes, F-35042, France

* corresponding author

alice.recanati@u-psud.fr

4 Tables

9 Figures

Submitted to Chemical Geology

Keywords: Apatite, Thermochronology (U-Th-Sm)/He, damage, trapping, diffusion

33

34

Abstract. Apatite (U-Th-Sm)/He (AHe) thermochronometry is widely used to constrain thermal histories and rates of tectonic, exhumation, and erosion processes. However, data interpretation is often challenging, especially when the thermal history includes extended residence time in the He partial retention zone (HePRZ), with highly dispersed dates revealing the complexity of diffusion processes in natural systems. This study investigates chemical and physical factors that may have impacted He diffusion in apatite over long timescales in a context of protracted residence in the HePRZ. Nine samples from the Ploumanac'h pluton and North Tregor (Armorican Massif, France) were collected in granitoids, differing in petrography and chemistry. This area was chosen because these samples underwent a similar thermal history since ~300 Ma. We report new (U-Th-Sm)/He dates, along with apatite fission-track (AFT) data, as well as lithological and chemical characterization. The results show dispersed (U-Th-Sm)/He dates, ranging from 87 ± 7 to 291 ± 23 Ma, whereas central AFT dates vary from 142 ± 6 to 199 ± 9 Ma. Current predictive models for He diffusion and fission-track annealing in apatite could not reproduce the two datasets together. However, this apparent discrepancy gives insight into the parameters influencing He diffusion at geological timescales. The data confirm that radiation damage enhances He trapping, as the AHe dates are positively correlated to effective uranium (eU) concentration. The He age dispersion for constant eU content cannot be explained just by variations in grain size or chemical composition. To explore the potential influence of recoil damage trapping behavior and annealing kinetics on AHe dates, we tested a new diffusion model from Gerin et al. (2017). Given the expected model of the thermal history provided by AFT inversion, we investigated the influence of the trapping energy on AHe dates. The AHe date variations can be explained only if the trapping energy evolves from one crystal to another, increasing with the amount of damage. For a given trapping energy, minor variations in the recoil-damage annealing rate can consistently explain most of the remaining dispersion of the AHe dates.

1. Introduction

Apatite (U-Th-Sm)/He (AHe) thermochronometry is widely used to determine the thermal histories of mountain ranges and sedimentary basins, as apatite crystals retain radiogenic helium at low temperature (<150°C) (e.g. House et al., 1998, Ehlers and Farley 2003, Stock et al., 2006; Reiners and Brandon, 2005, Valla et al., 2011; Herman et al., 2013).

(U-Th-Sm)/He thermochronometry is based on the accumulation of radiogenic ^4He in apatite crystals, generated by ^{238}U , ^{235}U and ^{232}Th alpha decay chains, and to a lesser extent by ^{147}Sm alpha decay. Interpretation of a set of AHe dates is not straightforward though, especially when the cooling history is complex or long (e.g. Green et al., 2006; Green and Duddy, 2006; Shuster et al., 2006; Lepretre et al., 2015) as this often produces high levels of intra and intersample dispersion. The extent to which such dispersion reflects complex He behavior during diffusion in apatite has yet to be fully explained.

Our knowledge of He diffusion in apatite has improved over the last decade due to numerous experiments and atomistic models (e.g. Farley 2000; Shuster et al., 2006; Cherniak et al., 2009; Bengston et al., 2012; Djimbi et al., 2015). In natural apatite, damage is produced during U-Th-Sm decay (alpha and recoil damage) and natural fission of ^{238}U and may undergo annealing (self repair) at elevated temperatures (Chaumont et al., 2002; Shuster and Farley, 2009). The level of preserved damage produced by alpha decay in an apatite can influence helium retention (reduced diffusion) due to the trapping of He atoms in the damaged areas which act as holes within the crystal structure (Shuster et al., 2006; Shuster and Farley, 2009; Gautheron et al., 2009; Gerin et al., 2017). Damage density depends on U-Th-Sm contents and on the damage-annealing rate, which varies with crystal chemistry and thermal history (Chaumont et al., 2002, Shuster and Farley, 2009; Gautheron et al., 2013, Fox et al., 2014).

Currently, two main models take into account the effect of damage trapping and

annealing on He retention in apatite (Flowers et al., 2009; Gautheron et al., 2009). Both models imply that the diffusion coefficient decreases with increasing damage fraction (or effective track density). Damage annealing is known to make the apatite lattice more diffusive for He atoms (Shuster and Farley, 2009), and has been suggested to be sensitive to apatite chemical composition as is fission track annealing (Gautheron et al., 2013). In the absence of specific damage annealing studies, alpha recoil damage and fission tracks are generally assumed to behave similarly. However, recent simulations from Fox and Shuster (2014) indicate that alpha damage may anneal slower than fission tracks.

Recently, a new radiation damage diffusion model was published by Gerin et al. (2017), and was implemented in QTQt for the purpose of our study. In this model, the closure temperature in undamaged apatite is assumed to be 30-40°C (Djimbi et al., 2015), and diffusion processes kinetics decrease with the alpha damage content as a function of damage retentivity. This last parameter is controlled by the trapping energy that adds to the activation energy, with a linear He trapping behavior.

Further work is required to better understand the long-term controls on helium retentivity in apatite, such as He damage trapping efficiency, the damage annealing rates, and the influence of microvoids in apatite (Zeitler et al., 2017). To this end, it is desirable to study the natural variability in helium dates (as in Green et al., 2006; Gautheron et al., 2009, 2013). Careful selection of apatite crystals is paramount for such work, as implantation, broken grains with mineral inclusions can also lead to significant scatter in AHe dates distribution (Vermeesh et al., 2007; Spiegel et al., 2009; Gautheron et al., 2012; Beucher et al., 2013; Brown et al., 2013; Murray et al., 2014; Janowski et al., 2017).

This study focuses on data from samples in the North Armorican Massif (western France), and particularly within the Ploumanac'h pluton and North Tregor massif. This region represents a single geological and tectonic domain and the samples experienced a common

thermal history since Carboniferous time. As the massif includes a variety of lithologies, the samples were selected specifically to assess whether petrography and apatite chemistry can account for the dispersion in the AHe datasets. The present work combines low temperature thermochronology, including apatite (U-Th-Sm)/He and fission-track analysis, and sample petrography/chemistry from the hand specimen to the mineral scale.

The aim of this study is to better understand the behavior of helium in apatite, as well as to test the current models for alpha damage accumulation and annealing. We first investigate the AHe date dispersion as a function of different physical and chemical parameters. Then, we try to model our dataset using the Flowers et al. (2009) and the Gautheron et al. (2009) models. We investigated the role of the damage retentivity and damage annealing kinetics to reproduce our dataset. To this aim, we used the new Gerin et al. (2017) model, as it is based on the most recent physical representation from Djimbi et al. (2015) and has a linear trapping behavior. We tweaked the trapping energy and damage annealing characteristics in order to predict our dataset. This approach give new insights into radiation damage and into the role of apatite chemistry on helium retentivity.

2. Geological setting

The Armorican Massif is located in northwestern France, bounded by the English Channel to the north, the Atlantic margin to the south, and the Paris Basin to the east (Fig. 1A). It is composed of Proterozoic and Paleozoic rocks that experienced the Cadomian and Variscan orogenic phases, respectively at 620-540 Ma and 416-299 Ma (Peucat, 1986; Pin and Peucat, 1986; Chantaine et al., 2001; Ballèvre et al., 2009). Large scale thrusting occurred along two NW-SE shear zones, dividing the massif into four main domains: the North, Central, and South Armorican zones, and the Leon domain to the north-west (Ballèvre et al., 2009). The Tregor unit lies in the North Armorican zone, and is delimited to the northwest by the Pink Granite Coast. The exposure along this coast reveals the Variscan

Ploumanach's pluton (303 ± 15 Ma, whole-rock Rb/Sr age, Vidal et al., 1981; 301 ± 1.7 to 309 ± 2.5 Ma, zircon U-Pb, Ballouard et al., 2015), emplaced within a Cadomian magmatic complex: the North Tregor batholith (~ 615 Ma), itself intruded within a ~ 2 Ga old Icartian host gneiss (U/Pb zircon ages; Auvray et al., 1980, Graviou, 1984), as illustrated in Fig. 1B.

This magmatic complex of the Ploumanach pluton is composed of three concentric bands (Barrière, 1977a; b): (i) the innermost two-mica granite and leucogranite (Fig. 1C, purple bands), (ii) a fine-grained granite (Fig 1C, orange band), and (iii) a coarse-grained pink granite (Fig. 1C, red band). The outermost pink granite grades from monzo- to syenogranite (Barrière 1977a; 1981). The outer two bands of magmatic rocks are co-genetic, formed during the initial magmatic injection (Barriere et al., 1977a). They were derived from a sub-alkaline magma, whereas the innermost white granites originate from the later cooling of a high-alumina magma, or from several non-cogenetic magma pulses (Albarède et al., 1980). The three concentric bands were emplaced at ~ 8 km depth (i.e. ~ 2 kbars, Barrière et al., 1977b), and now crop out due to significant erosion.

The absence of post-Variscan sedimentary deposits close to the studied area makes paleogeographic studies difficult. However, at a regional scale, the post-Variscan history of the Armorican Massif includes several geologically constrained phases of burial and erosion. During the Permian and Triassic the massif was exposed and the climate was arid, which favored fluvial and eolian sediment transport northward into depocenters (Owen, 1976; Ballèvre et al., 2012). These continental sediments are preserved in the northern seas (Western Approaches trough, English Channel) and onshore along the eastern margin of the Armorican Massif, nearby the Paris Basin. A marine transgression occurred during the Jurassic, and drowned most of the Armorican Massif. Evidence for this event is preserved in outcrops in the Normandy hills (Bessin et al., 2014), but also in offshore deposits in the Northern Approches Trough and adjacent basins (Menpes, 1997; Ziegler, 1987). A major

unconformity between Late Triassic and Jurassic deposits marks the initiation of this event, and is revealed by seismic data and well logs (Ruffell, 1995). Uplift in the early to mid-Cretaceous led to a second erosion phase (Owen 1976; Guillocheau et al., 2003), related to the rifting of the Bay of Biscay. It was possibly followed by a Upper Cretaceous marine transgression that is recorded by flints and chalk remnants (Hillis, 1991), followed by Pliocene sedimentation.

3. Sampling and methods

3.1. Sample collection and preparation

We collected nine samples to represent the natural chemical and lithological variation on the North Armorican massif, mostly on the Ploumanach pluton (Fig. 1B and C). Eight of the samples were selected out of a single intrusive body over a small geographic area (sampling interval: 1-2 km, area: 35 km²). Sample elevation is constant and low, as the pluton is close to sea level, and the pluton is not cut by any major fault. Therefore, the sampling procedure was designed so the sample thermal history should be similar for all of the samples. Any significant dispersion in AHe dates should thus be due to other causes (experimental, compositional, or other unknown other parameters).

The rocks (La Clarté and Traouieros granites) are porphyritic, with cm-size crystals. Five of the samples belong to the outermost band, i.e. the coarse-grained pink granites of “Traouieros” and “La Clarté” (samples PL1 to 4, and PL8, Fig. 1C, red band). Sample PL6 is similar to the “Traouieros” granites, but is part of an intrusion within the adjacent fine-grained band (Fig. 1C, orange band). Those granites include biotite and hornblende. The center of the pluton (Fig. 1C, purple bands) was also sampled, represented by sample PL7 (innermost leucogranite) and PL11 (two-mica granite). Both samples include biotite and muscovite. A single granodiorite specimen was also collected from the North Tregor batholith (PL10), located ~30km east of the Ploumanach pluton. Sample locations and petrography are reported

in Fig. 1B and C, and listed in Table 1.

Thin sections were prepared for each rock sample and apatite grains were separated using standard crushing, sieving, density and magnetic methods, and hand-picked using a binocular microscope. Apatite crystal selection for AHe and AFT analyses as well as apatite dissolution was performed at the GEOPS low temperature thermochronology laboratory (University of Paris Sud, France). U, Th, Sm, and major, trace and rare earth element (REE) composition was determined on the He dated apatite crystals at the LSCE (Gif sur Yvette, France). Major, trace, and rare earth element contents were determined on AFT dated grains and mounted apatite crystals, using electron microprobe and LA-ICPMS measurements performed respectively at at ISTERre (Grenoble, France) and UCL (London, UK).

3.2. Apatite fission track (AFT) analysis

Apatite grains were mounted in epoxy, polished, and etched at 5M HNO₃ for 20 seconds at 20±1 °C. AFT ages were obtained using the external detector method, following the zeta procedure (Hurford and Green, 1982). Analyst J. Barbarand's zeta value was 359±8 for the CN5 dosimeter glass. Apatite mounts were covered by muscovite external detectors, and irradiated at the Garching facility (München, Germany) with a nominal fluence of 5×10¹⁵ neutrons/cm². Detectors were subsequently etched for 20 minutes in 40% HF at 20±1°C. AFT ages are reported as the central age at ±1 σ (Galbraith and Laslett, 1996). Mean etch pit size (Dpar) was also measured. Tracks were counted and measured at x1250 magnification, using an optical microscope and a digitizing tablet (Laslett et al., 1994). Results are presented in Table 2.

3.3. Apatite (U-Th-Sm)/He dating

Apatite grains were carefully selected for AHe dating based on size, morphology, and on the absence of any optically detectable inclusion. Six to fifteen replicates per sample were analyzed. The analytical procedure is similar to that described by Gautheron et al. (2013)

Crystal dimensions were evaluated under a binocular microscope, and equivalent sphere radii (Rs) were calculated to represent the He diffusion domain (e.g. Gautheron and Tassan-Got, 2010). Ejection factors (F_T) were determined using Monte Carlo simulation (Ketcham et al., 2011; Gautheron et al., 2012). Individual grains were examined twice in order to check for any unrecognised He-rich inclusions.

U, Th and Sm concentrations were measured by isotopic dilution using a quadrupole ICP-QMS series^{II} CCT Thermo-Electron at the LSCE (Gif/Yvette, France). Apatite grains were dissolved in a HNO₃ solution spiked with ²³⁵U, ²³⁰Th, and ¹⁴⁹Sm. Analyses were calibrated using internal and external age standards, including Durango apatite and Limberg Tuff (Kraml et al., 2006; McDowell et al., 2005). Results of the Durango apatite are presented in supplementary information (Table S1). The one-sigma error on each AHe age amounts to 8%, reflecting the analytical error and the uncertainty on the ejection factor F_T correction. All AHe data are reported in Table 3, including the effective uranium concentration, ie. $eU = U + 0.24 \times Th$. Sm content was not measured in the first batch of grains (in italics in Table 3). For this dataset, the Sm content indicated in the table is the mean of the more recent analyses on the same sample. It was used for the (U-Th-Sm)/He date calculation. This approximation affects the AHe dates for the six grains with low eU (<20ppm), indicated by an asterisk in Table 3. However, the contribution of Sm on AHe dates is less than the analytical resolution for eU content higher than ~10 ppm (i.e. 8%). Additionally, three crystals showed anomalously high Th/U ratios compared to the other grains from the same sample, and will not be taken into consideration in this study, as the AHe dates may have been influenced by undetected U-Th rich inclusions such as thorite or uraninite, or incomplete apatite dissolution. When the AHe dates are used in order to compare to AFT data or to geological features, then it is appropriate to correct the AHe dates from the ejection factor F_T (Gautheron et al., 2012). This factor is computed from the crystal dimensions, and account for the fact that the helium

atoms located beneath the grain boundaries can be lost. Therefore, the correction aims at increasing the AHe in reason of this helium leak. Small crystals thus lose a larger proportion of helium during ejection than large grains and that's why the FT ejection factor depends on grain geometry. Note that in QTQt software, the entry parameter is the raw age, that we left in Figures 6, 7, and 8.

3.4. Major, minor and trace elements analyses

Apatite chemical composition was determined on some of the dated (U-Th-Sm)/He crystals, on AFT grain mounts and on some additional apatite fractions. The cation content of several individual (U-Th-Sm)/He dated apatite grains was quantified using the LSCE's quadrupole ICP-MS series^{II} CCT Thermo-Electron, including P, Ca, Mn, Sr, Ba, and REE. The measurements were performed on the same solutions previously used for U, Th, Sm analyses. Calibration was performed with internal and external standards that were analyzed several times during the experiment, similar to Cros et al. (2014). Reference material NIST 1640a and BCR (containing REE; Kent et al., 2007) were used for data validation. Relative standard deviation (RSD) on the NIST standard was <3%, except for P (15%). For REE, the RSD was remarkably low on BCR (0.5 to 2 %). Data treatment includes a correction regarding the reference values for NIST 1640, as well as a linear correction of the drift during the analytical sequences. Selected results can be found in Table 3, and all data can be found in supplementary Table (S2).

Fifty apatite grains per sample were selected and mounted in resin for Electron Probe Micro-Analysis (EPMA). The mean composition (in equivalent oxide weight percent) and standard deviations for each sample are reported in Table 4. Analyses were carried out at ISTERRE (Grenoble University, France), with a JEOL-JXA-8230 microprobe. Measurements included anions (F, Cl) and cations (Ca, P, S, Si, metals). Three repeated Durango measurements were made for standardization after 40 apatite grain analyses. Errors on

standards were relatively low for major elements: from 0.1% for CaO to 1.7 % for F <10% for all elements except Fe and Y (22 and 35%). Minor corrections were applied to account for the small drift in Ca and P. Counting errors on X-ray intensities were negligible for Ca, P, F, Si, Ce (<10%). Due to larger errors, Cl, Na, and La results are interpreted qualitatively.

Finally, the major, minor and trace element compositions of the AFT and AHe dated grains were also investigated. The AFT dated grains were analyzed using EPMA. Measurements were undertaken at ISTerre using a similar protocol to that described above, except that Pr was not analyzed. Additionally, three samples were analyzed using LA-ICPMS. Laser ablation was coupled to an ICPMS system (Agilent 7700) at UCL, London (UK) in order to determine the elementary concentrations in Mn, Sr, Ba, Nb, and rare earth element. Calibrations were based on external standards NIST 610 and 612 (Jochum et al., 2011).

4. Results

4.1 AFT data

AFT dating was performed for all samples except PL3 and PL8. The granite and granodiorite samples have similar AFT ages, with a central age ranging from 142 ± 6 to 199 ± 9 Ma (Fig. 1C). All samples passed the chi-square test at the 5% level, indicating that the range of single grain ages are consistent with a single population. Granitoid sample PL4 has a slightly older AFT age: 199 ± 9 (Table 2, Fig. 1C). Note that: (i) this sample has a similar Cl content than other samples, except PL10 that has slightly more Cl, (ii) PL4 is richer in Y and otherwise has a similar composition to the other samples (as well as a similar Dpar value).

Track length distributions are similar for all samples. Mean track length ranges between 12.5 ± 1.3 and 13.0 ± 1.2 μm (Fig. 1C, Table 2), with low standard deviation (<1.4 μm). Individual lengths vary between 8 and 16 μm , and the distribution of lengths is unimodal. The mean fission track-etch pit diameter (Dpar) ranges from 1.3 ± 0.1 to 1.5 ± 0.1 for all samples (Table 2). These values are quite low compared to those of Carlson et al. (1999),

yet they were cross-calibrated following a comparison with etching experiments in London, yielding a value of D_{par} of $1.5\ \mu\text{m}$ which is comparable to the values given by the theory of Carlson et al. (1999). Therefore, our D_{par} values are cross-calibrated and comparable to those given in Barbarand et al. (2003).

4.2 (U-Th-Sm)/He dating

Alpha ejection corrected (U-Th-Sm)/He dates for the nine samples range between 87 ± 7 and 291 ± 23 Ma. The effective uranium concentration (eU) is extremely variable from one grain to another, ranging from 1 to 557 ppm and the Th/U ratios also fluctuate, between 0.01 and 7.5. Apatite grain size, expressed as the equivalent spherical radius, varies between 34 and $105\ \mu\text{m}$, with a mean value of $59\ \mu\text{m}$.

AHe age dispersion correlates with eU (Fig. 2A): most AHe dates lie on a hyperbolic curve increasing with effective uranium (eU). Below the $eU=60\text{--}80$ ppm threshold, AHe rise with eU from 87 ± 7 Ma ($eU<2$ ppm) to >200 Ma. The granodiorite sample (PL10) has the youngest AHe dates and the lowest eU (<20 ppm). Compared to this end-member, the hornblende-bearing granite samples PL 2, PL 3, and PL 6 have older AHe dates (162 ± 13 to 250 ± 20 Ma; mean of 202 ± 22 Ma) and higher eU (44 to 326 ppm).

Some variations in (U-Th-Sm)/He dates appear to be independent of eU, as observed on Fig. 2A. For instance, for $eU\approx 80$ ppm (75-85 ppm), AHe are scattered between 178 ± 14 and 261 ± 21 Ma. This dispersion is observed even among different grains from the same sample. For instance, apatite crystals from sample PL2 range between 176 ± 14 and 234 ± 19 Ma.

4.3 Apatite geochemistry

The chemical composition of apatite crystals analyzed via EPMA is presented in Table 4 and Fig. 3. Results show an almost constant major element chemistry for all apatites: $\text{CaO}=54.2\pm 0.5\text{wt\%}$, $\text{P}_2\text{O}_5=41.1\pm 0.7\ \text{wt\%}$ and $\text{F}=3.7\pm 0.1\ \text{wt\%}$. In more detail, crystal

composition in CaO ranges from 52 to 56 wt%, with an approximately Gaussian distribution (Fig. 3A). P_2O_5 content lies between 39 and 44 wt%. Most crystals have F=3.4 to 3.9 wt% (Fig. 3B), except for sample PL11 which is F-rich (3.6 to 4.8 wt%). Note that the theoretical maximum F composition is 3.77 wt% assuming no Cl or OH and only Ca and P cations (Kecham, personal communication). This composition is very close to that of Durango apatite, as reported by Barbarand et al. (2003): CaO=54.7 wt%, P_2O_5 =41.2 wt%, and F=3.5 wt%.

Apatite crystals from the leucogranite (PL11) also have slightly different minor element chemistry, which results in a bimodal distribution of Fe, Mn, and Na (Fig. 3C and D). They contain higher Fe (0.4 ± 0.1 wt%), Mn (0.5 ± 0.1 wt%), and Na (0.12 ± 0.02 wt%) contents while being LREE-poor (e.g. Ce= 0.1 ± 0.03 wt%, Fig. 3E). Variations in sample lithology are accompanied by differences in apatite geochemistry: minerals from the different petrographic facies presented above (section 2) can be distinguished by their chemical composition (Fig. 3). Crystals from the granodiorite sample PL10 are characterized by high Cl contents (0.2 ± 0.1 wt%, Fig. 3F) and low F (3-3.8 wt%, Fig. 3B). They also have lower REE (e.g. Ce= 0.3 ± 0.04 wt%, Fig. 3E) than monzo and syenogranites. The apatite crystals in granitoid (PL4) are Na-rich (0.1 ± 0.03 wt%, Fig. 3C) and Y-rich (0.9 ± 0.3 wt%, Fig. 3H). Conversely, LREE contents are relatively low (e.g. La=0.1 wt%, Fig. 3G).

In addition to these measurements, we combined AHe dating and chemical analysis of sixty apatite crystals in order to enable direct comparison between AHe date and chemical composition. Results are included in Table 3. In general, there are no obvious chemical differences between the specimens. However, the pink granitoid PL4 is richer in REE than other samples with four crystals having $\Sigma REE > 3\%$ (cf. Table 3, where ΣREE is the sum of all analyzed REE). PL4 also has relatively low Sr contents (85-215 ppm). On the other hand, the granodiorite sample PL10 is Sr-rich (382-816 ppm) and ΣREE -poor (5730-10604 ppm).

Complete chemical contents can be found in supplementary information (Table S1, Figure S1).

5. Discussion

5.1. Variations in AHe dates

AHe dates vary between 85 ± 7 and 291 ± 23 Ma within the studied samples and seems to be controlled at first-order by the eU content (Fig. 2A). Additionally, the AHe dates can be plotted against the estimated alpha dose (Fig. 2B), which is the amount of alpha particles that were produced in apatite since the beginning of accumulation. This alpha dose was calculated from radionuclide concentrations, given the quantity of alpha particles produced by each radionuclides and the radioactive decay equation. We assumed that damage has accumulated for at least 250 Myrs, as the pluton likely was at too high temperature to accumulate damage before this date given the thermal history. 250 Myrs is also the oldest individual track dates, which indicate that the pluton was cold enough to retain tracks at this time.

On both figures, the AHe dates are broadly positively correlated with eU (for eU < 60-80 ppm) and alpha dose (below $\sim 2\text{-}3\times 10^{16}$ alpha/g). This confirms that crystal damage strongly controls He trapping in apatite. The present dataset highlights for the first time that the relationship between He retention and damage accumulation is more complex than assumed in current models (Flowers et al., 2009 and Gautheron et al., 2009).

Additionally, for a given range of eU, AHe dates appear to be strongly scattered (standard deviation of $\pm 20\%$ at ± 50 Ma). Another control mechanism is required to explain this scatter. Other factors than eU can be considered to influence He retention: (i) apatite crystal size, which controls the diffusion domain size (Reiners and Farley, 2001), (ii) grain morphology (Brown et al., 2013; Beucher et al., 2013), (iii) alpha implantation from rich U-Th neighbor minerals (Spiegel et al., 2009; Murray et al., 2014; Janowski et al., 2017), (iv) U

and Th zonation (Farley et al., 2011); Ault and Flowers 2012), and (v) apatite chemistry, more especially Cl content, which is often considered to control the damage annealing parameter by analogy with AFT studies (Ketcham et al., 2007; Gautheron et al., 2013), or (vi) apatite eU zonation, which might contribute to this dispersion.

No obvious relationship between AHe dates and apatite crystal size was found: we failed to evidence any correlation between AHe dates and crystal equivalent radius size (Fig. 4A), as the correlation coefficient is 0.04. Additionally, we examined whether a correlation exist within five restricted eU bins. The answer is negative: crystal size does not contribute to AHe data scatter. Results are presented in supplementary information. Thus crystal size does not directly influence He retention here. Note that apatites from the leucogranite (PL11), the two-mica granite (PL7), and the granitoid (PL4) are older than most apatites from monzo- and syenogranites (Fig. 2). Therefore, the variation in rock lithology seems to affect He date dispersion. Additionally there is dispersion in the apatite AHe dates from the same rock sample, e.g. PL2. Yet, at the 2σ uncertainty, most of these ages would be concordant. General influence of He implantation on AHe date dispersion is to rule out because thin section examination revealed no U-Th rich cluster around apatite. Thus, we rule out He implantation as a process that would have dispersed systematically the AHe dates within a sample.

We kept a record of 5 grain morphologies, as indicated in table 4B, following the number of pyramidal termination (0, 1, 2), and the number of broken faces (0, 1, or 2). There is no correlation between individual crystal AHe age and crystal length (Fig. 4B), and we observe no systematic trends with grain morphology. This absence of correlation is indicated by the fact that the correlation coefficient is nul, revealing that the crystal size and length do not influence significantly the AHe dates. We also showed that this correlation is absent for restricted eU bins. Thus, the crystal size does not control AHe dates. Additionally, we exclude

the hypothesis of helium implantation formulated here as explaining the whole AHe date dispersion. Indeed we examined sample thin sections which evidenced that apatite crystals are not close to U-Th rich mineral host and are not clustered. eU zonation could also induce a dispersion in AHe date, but not significant as no detectable zonation was noticed during AFT analysis.

5.2. AHe dates of highly damaged samples

The apatite crystals have eU ranging from 0 to 600 ppm. The high values of eU are quite rare, as usually it does not exceed 200 or 300 ppm. Additionally, the alpha doses range from 4×10^{15} to 5×10^{17} α/g , and thus exceed the usual range. For instance, Flowers et al. (2009) have investigated helium closure temperatures for apatites until 10^{17} α/g . Therefore, our set of apatite is interesting and rare in its chemical composition and damage content. Studying helium retention in those apatites, especially the most damaged apatite, is thus quite new and interesting.

Only a dozen of crystals have $eU > 150$ ppm and alpha doses $> 6 \times 10^{16}$ α/g so it is difficult to reach general conclusions about helium retention in highly damaged apatites. Yet, it is interesting to note that the mostly damaged apatites – from sample PL4 (557 ppm eU, and 5×10^{17} α/g) have low AHe dates (~ 152 Ma). This value is lower than the plateau age of 200-250 Ma reached by the apatites after the threshold of eU of 60 ppm (see the AHe vs eU plot in Figure 2A). Additionally, the ten crystals with the highest alpha doses ($> 6 \times 10^{16}$ α/g) have AHe dates decreasing with the alpha dose (Figure 2B). This negative correlation is confirmed by a relatively high correlation coefficient (~ 0.5). A figure is provided in the supplementary information for additional details (Figure S2), focused on these ten highly damaged apatites. Yet, this correlation coefficient is increased by the presence of the highest-alpha dose apatite.

Therefore, it is difficult to conclude because of the too small number of highly damaged apatites. But our dataset suggests that below a threshold of $2\text{--}3 \times 10^{16}$ α/g , helium retention increase with alpha doses while for higher values than 6×10^{16} α/g it decreases (Figure 2B). These preliminary observations should be confirmed by studying the AHe ages in more highly damaged apatites in different geological contexts. Yet, to our knowledge it is the first time that such a decrease in helium retention at high alpha doses is observed in apatite.

Note that in zircon, such phenomenon was already reported by Guenthner et al. (2013) and Ketcham et al. (2013). They proposed that beyond a certain alpha dose, alpha-recoil damage interconnect and He effectively percolates through zircon. Poor He retentivity in highly damaged zones is an expected characteristic of percolation. Therefore, if future works confirmed that it also occurs in apatite, then the increase in damage dose would cause damage to cluster at low alpha doses and then to percolate after a threshold dose.

5.3. AHe dates and apatite geochemistry

The geochemistry of apatite crystals can theoretically explain part of the AHe date dispersion via a change in He diffusivity (Wolf et al., 1998; Miro et al., 2006; Djimbi et al., 2015). However, no obvious relationship between individual grain age and chemistry was found. The only element whose concentration correlates with AHe dates is Sr (Fig. 5A). This inverse correlation is significant at the 5% level ($n=35$, correlation coefficient = -0.37). The two end-members are samples PL4 and PL10. Sample PL4 has high AHe dates (150 ± 15 to 280 ± 28 Ma) and low Sr contents (<211 ppm), and sample PL10 has low AHe dates ($<171 \pm 17$ Ma) and high Sr contents (>382 ppm). However, the correlation between AHe dates and Sr contents cannot be properly interpreted since Sr content is also inversely correlated with U content and eU (Fig. 5C), which is the main factor controlling helium retention rate. The

relationship between AHe dates and Sr is therefore most easily explained by the fact that both are correlated with U content (eU).

Similarly, ions that substitute for calcium in apatite may affect fission track annealing kinetics (Carlson et al., 1999; Barbarand et al., 2001; 2003; Ketcham et al., 2007). However, no clear correlation between date and chemistry was found for any other element. The correlation coefficients – which detect the presence of a correlation between two variables - often are null, as for Ba and La (Fig. 5B and D). This implies that major element substitution chemistry and AHe ages are independent. Therefore, we suggest that either there is no chemical control on AHe dates or the measured elemental concentrations do not vary enough to impact significantly the measured AHe dates.

Additionally, we were able to calculate the fission track annealing parameter $rmro$ from the entire chemical composition of the samples, estimated from EPMA measurements (from Ketcham et al., 2015). This parameter combines all chemical contents. Results are presented in supplementary information (Table S3). It reveals that only sample PL11 and PL4 have a slightly different value of $rmro$ (respectively 0.80 and 0.81), compared to other samples that have a higher value of $rmro$ (0.82-0.83). This is in agreement with the lithological difference that exists between both samples (a two-mica granite and a granitoid) compared to other samples that all are granites and granodiorite. It main explain some part of AHe dispersion (<50 Ma= 20%, as is illustrated in Figure 2A, the AHe dates of PL11 are slightly higher than those of pink granite samples). Nevertheless, there is an intrinsic dispersion in AHe dates within the pink granites (red dots), that cannot be explained by a variation in the chemical composition nor in the rmr_o parameter (which is 0.82).

5.4 (U-Th-Sm)/He dates simulation: insights into He behaviour in damaged apatite

5.4.1. Inconsistency between AFT and AHe dates

The (U-Th-Sm)/He dates are mostly older than AFT dates, except for sample PL10. We ran a series of inverse simulations of AHe and AFT date datasets together, using QTQt software (Gallagher et al., 2009; Gallagher, 2012). Inversion of the datasets was first performed without any constraints on the possible thermal history, given the formation age (~300 Ma). A second simulation was then carried out with one-single constraint at the time of rock formation: 300 Ma ago the pluton was at “higher temperature” relatively for the low temperature thermochronometers systems ($>200^{\circ}\text{C}$). A third simulation was performed, incorporating constraints based on the geological history described in section 2: (i) a Permian-Triassic exhumation phase to surface temperature, as the massif is known from independent geological to have been exposed emerged during this period, (ii) Cretaceous and Maastrichtian cooling at surface temperature, as the massif was uplifted during that time.

We tested both the Flowers et al. (2009) and the Gautheron et al. (2009) models. Both models suggest a reheating event in earliest Jurassic time. Based on the presence of Triassic detrital rocks ~180 km northwest of our study area (i.e Cotentin), and marine sediments in Normandy, Ballèvre et al. (2012) suggests that a denudation event occurred during the Triassic, followed by Jurassic reheating, as illustrated Figure 6A. This Triassic peneplanation event is classically described regionally in the Armorican Massif (Guillocheau et al., 2003), the Central Massif (Barbarand et al., 2001), and even North Africa (Gentil, 1912; Michard et al 2008). Either with or without geological constraints, none of these He diffusion models reproduce both the AHe and AFT datasets. More specifically, the old AHe dates cannot be explained given the AFT dates. The models underestimate the AHe dates, and overestimate the AFT dates. Several examples of these inverse model results are provided in the supplementary section (Fig. S3 and S4).

We thus decided to construct a geological plausible thermal history by inverting only the AFT dataset, using the geological constraints (Black boxes in Fig. 6A). In doing this, we

assume the fission track inversion technique is reliable, as it has been improved since 30 years, although innovations in fission track analysis can still be carried out. We use the most recent track annealing model implemented in QTQt (Ketcham et al., 2011), which we assume is enough constrained for the purpose of our study. The aim of our paper is not to discuss the regional thermal history nor the fission track annealing kinetics, but rather to use a reasonable T-t path in order to improve the (U-Th-Sm)/He techniques.

Four geological constraints were used: (i) the pluton was emplaced at high pressure and temperature 300 Ma ago (box 1, Fig. 6A; Barrière et al., 1977a), (ii) the rock was at near surface temperature during the Triassic (box 2), and the Maastrichtian, (iii) the pluton has been at surface temperature for less than 50 Ma (box 4). The present day temperature was also set at $10\pm 10^{\circ}\text{C}$. Box 3 results from a thermochronometric constraint: as the samples were not entirely annealed, the rock did not exceed 110°C . QTQt enabled the fission track diameter D_{par} to vary. AFT annealing parameter was calculated for each grain from these values.

Figure 6A present the result of the inversion of all samples analysed for fission-tracks (ages and lengths). It is a set of possible T-t paths, with different probabilities given the dataset. The most probable T-t paths are represented in red, while the less probable are in blue (Fig. 6A). We decided to select the “expected model” (black line in Fig. 6A) as our preferred thermal history, as this history represents a weighted model (Gallagher 2012, 2015), which is the most probable given the AFT dataset. For information, the “maximum likelihood” model was very similar to the “expected” model. In the supplementary information, we added a comparison of the predicted ages and the observations for different (T-t) paths (Figure S5). The less probable paths (in blue in Figure 6A) do not reproduce the AFT ages. Only the expected model fits several of the AFT dates. Figure 6B represent the predicted AFT ages against the observations for the expected model (green squares). The expected model fits the highest dates around 180-200 Ma, but slightly overestimates the lowest range of AFT dates

(140-150 Ma).

The numerical inversion of the samples with lowest dates (e.g.: PL1 only) was also performed with AFT ages only, and with ages and lengths. Both simulations provide the same thermal history, which are presented in supplementary information (Figure S6). It evidences that in order to reproduce the lowest dates, the Jurassic heating has to be 110°C if we inverse only PL1. Figure 6B presents the predicted fission track ages for this thermal history (yellow square). The younger AFT ages (140-180 Ma) are reproduced, but the highest AFT date (200 Ma) is slightly underestimated.

Nevertheless, as all samples were collected over a small (km^2 scale) area, which is not crosscut by any major fault, and at the same elevation, all of the samples underwent the same thermal history (and so the same Jurassic heating). For instance, sample PL1 and PL2 are separated from only 200 m and have undergone a similar geological and thermal history, but have AFT ages differing by 45 Ma. No particular chemical feature appears to distinguish PL1 and PL2, and their resulting annealing parameter calculated from Ketcham et al. (2015) is similar (0.82). The difference in AFT ages thus likely evidences that other parameters than the thermal history and the apatite chemical composition influence the fission track annealing kinetics. As it is not taken into account yet in fission track models, we will not be able to reproduce both the highest and the lowest AFT ages with a single thermal history. We decided to reproduce the highest dates around from Siddall 1993; 207 ± 9 Ma for PL-14-1 from Ballouard et al. 2015). Therefore, in the following, the expected model presented in Figure 6A will be used.

The expected thermal history model was used for a series of forward simulations of the dataset. These simulations reproduced the oldest AFT data correctly according to HeFTy (Ketcham, 2005) and QTQt (Gallagher 2012) simulations. However, our forward simulations cannot explain the AHe data given the chosen Tt path. Given the Flowers et al. (2009) and the

Gautheron et al. (2009) models, the predicted AHe versus eU relationship is not consistent with the observations: both models underestimate the AHe dates (see figure 6C and 6D, green squares).

We also tested the sensitivity of the forward simulations for variation in the maximum Jurassic temperature. Figure 6B represent the AFT dates and Figure 6C and 6D are the AHe vs eU relationship predicted for a Jurassic burial temperature of 80°C (red triangles) compared to the expected heating of 130 °C (green squares). The results show that even though AFT dates are strongly dependent on the heating temperature (see Figure 6B), the AHe dates are not. The simulations performed with a higher Jurassic burial temperature are slightly lower, but this does not affect significantly the AHe vs eU relationship (Figure 6C and 6D).

If we inverse the AHe dataset without AFT constraints, the expected Jurassic burial temperature is 50°C using both the Flowers et al. (2009) model and the Gautheron et al. (2009) model (see Figure S7 and S8 in supplementary data. Nevertheless, if we reduce the Jurassic burial temperature from 130 to 80°C, the helium retention slightly increase but not enough to reproduce the modeled AHe/eU curve (Figure 6C and 6D). Additionally, with a 50°C burial temperature, the simulated AFT ages would be significantly older than measured (205-220 Ma vs 140-200 Ma). With a 40°C reheating, as suggested by the Gautheron et al. (2009) model, the AFT ages would even range from 230 to 250 Ma (forward simulations). Therefore, whatever the thermal history is selected, the current models underpredict helium retention and cannot reproduce the observations. Even excluding the fission track lengths, we cannot reproduce both AFT and AHe dates given a single thermal history.

To summarise, neither of the current damage accumulation and annealing models for apatite can reconcile both thermochronological datasets. Inversion of AFT and AHe dates failed to reproduce AFT and AHe data together. The old AHe dates compared to AFT dates

indicate that: (i) the AHe system records earlier parts of the thermal history than AFT, and (ii) He retention in apatite is high, revealing that damage annealing is probably slow or that damage retention is high. Thus, the parameters used in the current models to describe helium retention (e.g. activation energy) and damage annealing kinetics do not manage to predict helium retention.

5.4.2. Reconciling AFT and AHe datasets: a new model

Failure to produce thermal history models that fit both the AFT and AHe data suggest that either the AFT models are wrong or, as already mentioned in section 5.1, He behaviour in apatite is more complex than described by previous models (Gautheron et al., 2009; Flowers et al., 2009). To investigate He trapping in apatite, and its evolution with the damage dose, the recent He diffusion model from Gerin et al. (2017) was implemented in the QTQt software. This recent model has the advantage that the helium retention efficiency can be easily modified by the user, through a parameter called the trapping energy ΔE_a .

In their contribution, Gerin et al. (2017) propose a relationship between radiation damage accumulation and the diffusion properties, where the diffusion coefficient \tilde{D} decreases with the damage fraction $f(x)$ following the equation:

$$\tilde{D}(x,t) = \frac{D(T)}{\left[1 + f(x) \exp\left(\frac{\Delta E_a}{RT}\right) h\right]} \quad (1),$$

where $D(T)$ is the diffusion coefficient in undamaged apatite; ΔE_a is the additional energy that is required for He, once it has entered into a damage site, to diffuse back into the lattice (see Shuster et al., 2006; Gautheron et al., 2009); and h is the percentage of annealing ranging from 0 to 1. In the Gerin et al. (2017) model, initial He diffusion parameters (diffusion coefficient D_0 and activation energy E_a) are adopted from multi scale quantum based Density Function Theory (DFT) calculations (Djimbi et al., 2015). Such calculations yield a He closure temperature of $\approx 30-40$ °C for undamaged apatite.

Here, we used the same approach but the alpha damage annealing parameter is hereafter termed rmr_0' , to distinguish it from the rmr_0 parameter used to describe AFT. This new parametrization of rmr_0' may help to reconcile AFT and AHe data (Fox and Shuster, 2014), which was not possible in previous models that considered that track and recoil damage anneal at the same rate (i.e. $rmr_0=rmr_0'$). Following Ketcham et al. (2007), the value of rmr_0 can be calculated either from the Dpar measurements, or from the Cl content, and varies between 0.6 and 0.83 in most natural apatites, even though in rare crystals it goes down to 0. In the case of the Ploumanac'h rocks, the rmr_0 value calculated from Dpar values is 0.85 (Ketcham et al. 2007), while that calculated from the Cl PFU contents, issued from EMP analyses is 0.83, except for sample PL10 (0.82). More recently, Ketcham et al. (2015) propose that rmr_0 is multi-compositional. We calculated the values of rmr_0 using this recent study: 0.82-0.83 for all samples except PL11 (0.80), PL4 (0.81). Results can be found in supplementary informations. Unfortunately, we did not analyze sample PL7, that likely has a different composition due to its lithological specificity.

5.4.3. Investigation of damage trapping energy (ΔEa)

We first estimate the range of trapping energy ΔEa that is required to reconcile the AHe with the thermal history obtained from AFT data and assumed geological constraints. The ΔEa value depends on damage topology, i.e damage shape, size, and connectivity. In the case of simple vacancies, Gerin et al. (2017) estimated that ΔEa is $\sim 30 \pm 5$ kJ/mol, based on DFT calculations. Shuster and Farley (2009) also predict experimental values in the same order of magnitude (~ 25 kJ/mol). In addition, Gerin et al. (2017) suggest that damage clustering increases ΔEa to higher than 50 kJ/mol.

Using our preferred thermal history (Fig. 6A), we ran several forward simulations in which we vary the damage trapping energy ΔEa from 30 to 90 kJ/mol. Results are

summarised in Fig. 7, where the AHe vs eU relationship was modeled for different values of ΔEa . With $\Delta Ea=30$ kJ/mol (red triangles) or 40 kJ/mol (yellow losangles), the predicted AHe dates are significantly lower than observed values (Fig 7A) so these trapping energies are not sufficient to retain enough helium. However, for the trapping energy ΔEa of 70 kJ/mol (green squares), the model dates better fit the mean observed AHe dates (blue circles).

Note that for the lowest eU values ($eU < 20$ ppm), the trapping energy of 70 kJ/mol overestimate the AHe dates, while for higher eU values it correctly reproduce the observations. Thus, the whole data dispersion cannot be reproduced if all of the crystals have the same ΔEa value. Therefore, we decided to vary the ΔEa value for each grain from samples PL10 and PL4, i.e. samples with the lowest and the highest eU. The results are presented in Fig. 7B and 7C. For each crystal, we determined the ΔEa value required so that the predicted AHe agrees reasonably well with the measured AHe date so that in a prediction vs. observation diagram, the data points lie around the 1:1 straight line (Figure 7B and 7C). ΔEa values are represented on a color scale from pink to red, and are indicated on the plots. Please remind that these simulations were performed using one single Tt path, the “expected model” that fits AFT dates. At this stage, the rmr_0' parameter was chosen equal to rmr_0 ($=0.81$ and 0.82), calculated from the chemical composition measurements (using Ketcham et al., 2015). We will come back to the role of a variable rmr_0' later.

For sample PL10, the simulation showed that the required ΔEa is relatively high ($46 < \Delta Ea < 87$ kJ/mol), given the assumption made and the chosen thermal history. Additionally, ΔEa is the main parameter to increase the predicted AHe date, and thus it increases with the measured AHe date (Fig. 7C, purple to red triangles). As AHe positively correlates with eU in PL10, ΔEa also increases with damage density (Fig.8). Damage clustering (recombination, or gathering) may explain this implied increase in trapping energy.

This can be inferred from our understanding of the diffusion process at atomic scale: helium migration between sites is restricted due to its repulsion by neighbour atoms. To overcome this effect, helium atoms have to provide an additional energy. The energy that needs to be furnished in order to fit an atom (or one mole) of helium from outside of the crystal into an insertion site is called the “insertion energy” which amounts to 0.66 eV (Djimbi et al., 2015) in apatite, i.e. 64 kJ/mol. Extended damage, like cavities, are zones where the neighbor atoms are distant. Therefore, the repulsion effect drops, and the energy barrier height equals the insertion energy. On the other hand, small damage sites are neighboured by repelling atoms, which favors helium jump to another site. The energy barrier is thus smaller than for larger damage sites. ΔEa quantifies the increase in the required energy barrier induced by a defect. This rise in energy is caused by the increase in the distance between helium and neighbour atoms that reduce the repulsion effects. Depending on the size of the defect site, the value of ΔEa ranges from 0 kJ/mol (no trapping effect in small-size defect site with high repulsion effects) to 64 kJ/mol (large cavities, with efficient trapping). This range of values is also documented in the DFT calculation in the Gerin et al. (2017) study, where the values of ΔEa (20-50 kJ/mol) are beyond the insertion energy. Note that if the interaction between helium and neighbour atoms was attractive at moderate distance, the ΔEa values could theoretically be higher than the insertion energy.

5.4.4. Investigation of alpha recoil damage annealing behaviour

In this section, we used a similar approach, but kept the ΔEa value constant, and investigated the rmr_0' values required to reproduce AHe dates. Fig. 9A and 9B present the results of two simulations, performed with rmr_0' value of 0.7 and 0.9 (red triangles and green squares respectively), all other parameters being constant ($\Delta Ea=40$ or 70 kJ/mol). For AFT analysis, rmr_0 is 0.8-0.83, but we explore here any other variation of rmr_0' . The modeled AHe are negatively correlated to rmr_0' (red triangles are above green squares). This is consistent, as

alpha-recoil annealing enhances He diffusion (Gautheron et al., 2009; Shuster and Farley, 2009).

As is revealed by Figure 9A, except for low eU values, the AHe vs eU relationship is better reproduced with $\text{rmr}_o'=0.7$ (red triangles) than with $\text{rmr}_o'=0.9$ (green squares). This reveals that alpha-recoil damage likely anneal slowly – maybe more slowly than fission tracks-, as suggested by Fox and Shuster (2014). Note that a high trapping energy is required, as otherwise the observed AHe vs eU relationship would not be reproduced (Figure 9B). Therefore, the conclusions of section 5.4.3 still stand.

5.5. Implications regarding He trapping law

The trapping energy (ΔEa) quantifies the damage topology as it increases with the damage site size and when defects cluster as proposed by Gerin et al. (2017). As illustrated in Fig. 8, the present study suggests that – given the assumption made and the chosen expected Tt path – a positive correlation between ΔEa and eU can explain the data at low eU (in the sample PL10). The conclusions from all the parameter tweaking (ΔEa and rmr_o') is that in order to reproduce both the AHe and the AFT dataset the trapping energy has to be high enough (>46 kJ/mol) and to vary between crystals. This is the main difference between the Gerin et al. (2017) model and other radiation models: in QTQt, other radiation models such as the Flowers et al. (2009) or Gautheron et al. (2009) model consider that the activation energy is constant for all crystals. Within the Gerin et al. (2017) model, the trapping energy can be varied between grains, and that's why we can reproduce our dataset.

Our study suggests that this trapping energy increases with the alpha dose below a threshold. It may reveal that: (i) in low damaged apatites, defect clustering occurs with dose accumulation, while (ii) after a damage dose threshold is reached, the damage site size declines or defect declustering occurs. Defect clustering in low damaged apatites likely leads to an increase in He retentivity, due to the creation of microvoids in apatite (Zeitler et al.,

2017). The geometry of damaged zones may be drastically modified in highly damaged apatites, as already mentioned earlier. If this were also a significant process for high eU apatite, the damage accumulation physics of Gerin et al. (2017) would not be applicable, and another model should be elaborated specifically for highly damaged samples.

6. Conclusion

Our study investigated variations in (U-Th-Sm)/He date from samples with differing chemistry and petrography, which have undergone a protracted low temperature thermal history. Fission track analysis and geological constraints show that the samples were first exhumed after the Variscan orogeny, and then were buried until 110°C during the Jurassic, before being exhumed once more. Our study investigated some parameters that have the potential to influence He diffusion in apatite.

Results show dispersed (U-Th-Sm)/He dates, ranging from 80 ± 8 to 291 ± 29 Ma, which are mostly older than the central AFT dates (142 ± 6 to 199 ± 9 Ma). In detail, the (U-Th-Sm)/He dates increase with the effective uranium content (for $eU < 60$ -80 ppm) and effective recoil track density ($< 2\text{-}3 \times 10^{16}$ alpha/g). This confirms that crystal damage strongly controls He trapping in apatite. For higher alpha doses, ten crystals preliminarily suggest a decrease in helium retention above a threshold in damage content; but this should be investigated further by future works. Apatite grain chemistry was also investigated to test its potential impact on AHe dates. Our data suggest that either there is no chemical control on AHe dates or our measured elemental concentrations do not vary enough to impact significantly on the measured AHe dates.

Current He radiation damage models fail to reproduce the present dataset adequately and they cannot reconcile the apparent discrepancy between AFT and AHe dates. To determine whether this discrepancy can be resolved we implemented the recent He diffusion model by Gerin et al. (2017) and an alpha damage annealing law similar to the Ketcham et al.

(2007)'s model for fission tracks. We tested the sensitivity of the model to variations in alpha recoil damage trapping energy (ΔEa) and annealing kinetics. Thus, we determined the ΔEa and rmr_0 parameters required to reproduce the data. $Rmro$ characterizes annealing kinetics of alpha damage. (U-Th-Sm)/He and AFT dates can be adequately modeled together using (i) enhanced trapping, or (ii) reduced annealing (or a combination of both). The first mechanism requires high damage trapping energy values (ΔEa of 40-80 kJ/mol), which exceeds estimates for a single vacancy from DFT calculations (~30 kJ/mol). This may be understandable if the accumulated individual damage sites coalesce to form single connecting vacancies, thereby creating extended damaged domains.

For high alpha doses, if the decrease of AHe dates is confirmed by future works, then we suggest a similar behavior than previously described in zircon by Ketcham et al. (2013), involving topological modification or damage interconnection. Variations in annealing kinetics induce some dispersion in AHe dates, but cannot explain the observed AHe scattering without any change in damage trapping energy. The second key point revealed by the samples from Tregor is that alpha recoil probably anneals slower than fission tracks. Future models should take this into consideration and investigate damage annealing mechanisms.

Acknowledgments

Julien Beucher is thanked for his participation in apatite picking and sample preparation for U-Th measurements. Ludovic Lafforgue is gratefully thanked for help during density separation and AHe analysis at GEOPS, and Remi Leprêtre for insightful discussions. Valentina Batanova is acknowledged for EPMA analyses at ISTERre, and Martin Richter for his help during trace elements analysis at UCL, London. Barry Kohn, Richard Ketcham, and an anonymous reviewer greatly improved the manuscript by their insightful comments. This work is part of the ANR-12-BS06-0005 HeDiff project.

References

Albarède F., Dupuis C., Taylor Jr H.P., 1980. $^{18}\text{O}/^{16}\text{O}$ evidence for non-cogenetic magmas associated in a 300 Ma old concentric pluton at Ploumanac'h (Brittany, France). J. Geol. Soc. 137: 641-647.

- Ault A., Flowers R.M., 2012. Is apatite U-Th zonation information necessary for accurate interpretation of apatite (U-Th)/He thermochronometry data? *Geochim. Cosmochim. Acta* 79: 60-78.
- Auvray, B., Charlot, R., Vidal P., 1980. Nouvelles donnees sur le proterozoique inferieur du domaine nord Armoricaire (France): âge et signification. *Revue canadienne des Sciences de la Terre* 17: 532-538.
- Ballèvre, M., Bosse, V., Ducassou, C., Pitra, P., 2009. Palaeozoic history of the Armorican Massif: models for the tectonic evolution of the suture zones. *C.R. Geoscience* 341: 174-201.
- Ballèvre, M., Bosse, V., Dabard, M.P., Ducassou, C., Fourcade, S., Paquette, J.L., Peucat, J., Pitra, P., 2012. Histoire geologique du Massif Armoricaire: actualite de la recherche. *Bull. Soc. Geol. Mineral. Bretagne*, 10-11: 5-96.
- Ballouard, C., Poujol, M., Jolivet, M., Boulvais, P., Tartese, R., Dubois, C., Hallot, E., Dabard, M.P., Ruffet, G., 2015. Geochronological and thermochronological constraints on the Carboniferous magmatism from the Armorican Massif: from the source to the exhumation. Conference poster. Variscan 2015, Jun 2015, Rennes, France.
- Barbarand, J., Pagel, M., 2001. Contrôle de la cicatrization des traces de fission dans les cristaux d'apatite: le rôle de la composition chimique. *C.R. Acad. Sci. Paris*. 332: 259-265.
- Barbarand, J., Carter, A., Wood, I., Hurford, T., 2003. Compositional and structural control of fission-track annealing in apatite. *Chem. Geol.*, 198: 107-137.
- Barbarand J., Lucazeau F., Pagel M., Séranne M., 2001. Burial and exhumation history of the south-eastern Massif Central (France) constrained by apatite fission-track thermochronology. *Tectonophysics* 335: 275-290.
- Barrière, M., 1977a. Deformation associated with the Ploumanac'h intrusive complex, Brittany. *J. Geol. Soc.* 134: 311-324.
- Barrière, M., 1977b. Le complexe de Ploumanac'h, Massif Armoricaire. Essai sur la mise en place et l'évolution pétrologique d'une association plutonique subalkaline tardi-orogénique. PhD. Université de Brest.
- Barrière, M., 1981. On Curved Laminae, Graded Layers, Convection Currents and Dynamic Crystal Sorting in the Ploumanac'h (Brittany) Subalkaline Granite. *Contrib. Min. Petrol.* 77: 214-224.
- Bengtson A., Ewing, R.C., Becker U., 2012. He diffusion and closure temperatures in apatite and zircon: a density functional theory investigation. *Geochim. Cosmochim. Acta* 86: 228-238.
- Bessin P., Guillocheau F., Robin C., Schrötter J.M., Bauer H., 2014. Planation surfaces of the Armorican Basin (Western France): Denudation chronology of a Mesozoic land surface twice exhumed in response to relative crustal movements between Iberia and Eurasia. *Geomorphology* 233:75-91.
- Beucher, R., Brown, R.W., Roper S., Stuart, F., Persano, C., 2013. Natural age dispersion arising from the analysis of broken crystals. Part II. Practical application to apatite (U-Th)/He thermochronometry. *Geochim. Cosmochim. Acta* 120: 395-416.
- Brown R.W., Beucher R., Roper S., Persano C., Stuart F., Fitzgerald P., 2013. Natural age dispersion arising from the analysis of broken crystals. Part I: Theoretical basis and implications for the apatite (U-Th)/He thermochronometer. *Geochim. Cosmochim. Acta* 122: 478-497.
- Carlson, W.D., Donelick, R.A., Ketcham, R.A., 1999. Variability of apatite fission-track annealing kinetics: I. Experimental results. *Am. Min.* 84: 1213-1223.

- Chantraine, J., Egal, E., Thieblemont, D., Le Goff, F., Guerrot, C., Ballevre, M., Guennoc, P., 2001. The cadomian active margin (North Armorican massif, France): a segment of the North Atlantic Panafrican belt. *Tectonophysics* 331: 1-18.
- Chaumont, J., Soulet, S., Krupa, J.C., Carpéna, J., 2002. Competition between disorder creation and annealing in fluoroapatite nuclear waste forms. *J. Nuc. Mater.* 301: 122-128.
- Cherniak D.J., Watson E.B., Thomas J.B., 2009. Diffusion of helium in zircon and apatite. *Chem. Geol.* 268: 155-166.
- Cros A., Gautheron C., Pagel M., Berthet P., Tassangot L., Douville E., Pinna-Jamme R., Sarda P., 2014. ⁴He behavior in calcite filling viewed by (U-Th)/He dating, ⁴He diffusion and crystallographic studies. *Geochim. Cosmochim. Acta* 125: 414-432.
- Djimbi, D., Gautheron C., Roques, J., Tassan-Got, L., Gerin, C., Simoni, E. 2015. Impact of apatite chemical composition on (U-Th)/He thermochronometry: an atomistic point of view. *Geochim. Cosmochim. Acta* 167: 162-176.
- Ehlers, T.A., Farley, K.A., 2003. (U-Th)/He thermochronometry: methods and applications to problems in tectonic and surface processes. *Earth Planet. Sci. Lett.* 206: 1-14.
- Farley, K., 2000. Helium diffusion from apatite: general behavior as illustrated by Durango fluoroapatite. *J. Geophys. Res.* 105: 2903-2914.
- Farley, K.A., Shuster D.L., Ketcham R.A., 2011. U and Th zonation in apatite observed by laser ablation and implications for the (U-Th)/He system. *Geochimica et Cosmochimica Acta* 75: 4515-4530.
- Flowers, R., Ketcham, R.A., Shuster, D., Farley, K.A., 2009. Apatite (U-Th)/He thermochronology using a radiation damage accumulation and annealing model. *Geochim. Cosmochim. Acta* 73: 2347-2365.
- Fox M., Shuster, D.L., 2014. The influence of burial heating on the (U-Th)/He system in apatite: Grand Canyon case study. *Earth Planet. Sci. Lett.* 397: 174-183.
- Galbraith, R. F., Laslett, G. M. 1993. Statistical models for mixed fission track ages, *Nucl. Tracks Radiat. Meas.* 21: 459-480.
- Gallagher, K., Charvin, K., Nielsen, S., Sambridge, M., Stephenson, J., 2009. Markov chain Monte Carlo (MCMC) sampling methods to determine optimal models, model resolution and model choice for Earth Science problems. *Marine and Petroleum Geology* 26: 525-535.
- Gallagher, K., 2012. Transdimensional inverse thermal history modelling for quantitative thermochronology. *J. Geophys. Res.* 117 (B02408): 16pp.
- Gallagher, K., 2015. QTQt 5.4.3. user guide.
- Gautheron, C., Tassan-got, L., Barbarand, J., Pagel, M., 2009. Effect of alpha-damage annealing on apatite (U-Th)/He thermochronology. *Chem. Geol.* 266: 166-179.
- Gautheron, C., Tassan-Got, L., 2010. A Monte Carlo approach of diffusion applied to noble gas/helium thermochronology. *Chem. Geol.* 273: 212-224.
- Gautheron, C., Tassan-got, L., Ketcham, R.A., Dobson, K.J., 2012. Accounting for long alpha-particle stopping distances in (U-Th-Sm)/He geochronology: 3D modeling of diffusion, zoning, implantation, and abrasion. *Geochim. Cosmochim. Acta* 96: 44-56.
- Gautheron, C., Barbarand J., Ketcham R., Tassan-Got L., van der Beek P., Pagel M., Pinna-Jamme R., Couffignal F. and Fiallin M., 2013. Chemical influence on α -recoil damage annealing in apatite: implications for (U-Th)/He dating. *Chem. Geol.* 351: 257-267.
- Gentil L., 1912. La Géologie du Maroc et la genèse de ses grandes chaînes. In: *Annales de Géographie*, t. 21, no 116, pp. 130-158.
- Gerin, C., Gautheron, C., Oliviero, E., Bachelet, C., Djimbi, M.D., Seydoux-Guillaume, A.M., Tassan-Got, L., Sarda, P., Roques, J., Garrido, F. Influence of vacancy damage

- on He diffusion in apatite, investigated at atomic to mineralogical scales. *Geochim. Cosmochim. Acta.* 197: 87-103.
- Graviou, P., 1984. Petrogenese des magmas calco-alkalins: exemple des granitoïdes cadomiens de la region Tregorroise (Massif Armoricaïn). PhD, University of Rennes 1.
- Green, P.F., Crowhurst, P.V., Duddy, I.R., Jaspén, P., Holford, S.P., 2006. Conflicting (U-Th)/He and fission track ages in apatite: Enhanced He retention, not annealing behaviour. *Earth Planet. Sci. Lett.* 250: 407-427.
- Green, P.F., Duddy, I.R., 2006. Interpretation of apatite (U-Th)/He ages and fission track ages from cratons. *Earth Planet. Sci. Lett.* 244: 541-547.
- Guenther, W.R., Reiners P.W., Ketcham R.A., Nasdala L., Giester G., 2013. Helium diffusion in natural zircon: radiation damage, anisotropy, and the interpretation of zircon (U-Th)/He thermochronology. *Am. J. Sci.* 313: 145-198.
- Guillocheau, F., Brault, N., Thomas, E., Barbarand, J., Bonnet, S., Bourquin, S., Esteoule-Choux, J., Guennoc, P., Menier, D., Neraudeau, D., Proust, J.N., Wyns, R., 2003. Histoire geologique du Massif Armoricaïn depuis 140 Ma (Cretace-Actuel). *Bulletin d'information des geologues du Bassin de Paris* 40: 13-28.
- Herman F., Seward D., Valla P.G., Carter A., Kohn B., Wilett K.S.D., Ehlers T.A., 2013. Worldwide acceleration of mountain erosion under a cooling climate. *Nature* 504: 423-426.
- Hillis, R.R., 1991. Chalk porosity and Tertiary uplift, Western Approaches Trough, SW UK and NW French continental shelves. *J. Geol. Soc., London* 148, 669-679.
- House M.A., Wernicke B.P., Farley K.A., 1998. Dating topography of Sierra Nevada, California, using (U-Th)/He ages. *Nature*, 396: 66-69.
- Hurford A.J., Green P., 1982. A users' guide to fission track dating calibration. *Earth Planet. Sci. Lett.* 59: 343-354.
- Janowski, M., Loget, N., Gautheron, C., Barbarand, J., Bellahsen, N., Van den Driessche, J., Babault, J., Meyer, B., 2017. Neogene exhumation and relief evolution in the eastern Betics (SE Spain): insights from the Sierra de Gador. *Terra Nova* 29, 91-97.
- Jochum, K.P., Weis U., Stoll B., Kuzmin D., Qichao Y., Raczek I., Jacob D.E., Stracke A., Birbaum K., Frick D.A., Günther D., Enzweiler J., 2011. Determination of reference values for NIST SRM 610-617 glasses following ISO guidelines. *Geostandards and Geoanalytical Research* 35: 397-429.
- Kent A.J.R., Jacobsen B., Peate D.W., Waigh T.E., Baker, J.A., 2007. Isotope dilution MC-ICP-MS rare earth element analysis of geochemical reference materials NIST SRM 610, NIST SRM 612, NIST SRM 614, BHVO-2G, BCR-2G, JB-2, WS-E, W-2, AGV-1, and AGV-2. *Geostandards and Geoanalytical research*, 28: 417-429.
- Ketcham, R.A., 2005. Forward and inverse modelling of low-temperature thermochronology data. In: Reiners P.W and Ehlers T.A. (Ed.) *Low temperature thermochronology: techniques, interpretations and applications. Reviews in mineralogy and geochemistry*, 275-314.
- Ketcham, R.A., Carter, A., Donelick, R.A., Barbarand, J., Hurford, A.J., 2007. Improved modeling of fission-track annealing in apatite. *Am. Min.* 92: 799-810.
- Ketcham, R.A., Gautheron, C., Tassan-got, L., 2011. Accounting for long alpha-particle stopping distances in (U-Th-Sm)/He geochronology: refinement of the baseline case. *Geochim. Cosmochim. Acta.* 75: 7779-7791.
- Ketcham, R.A., Guenther W.R., Reiners P., 2013. Geometric analysis of radiation damage connectivity in zircon, and its implications for He diffusion. *Am. Min.* 98: 350-360.
- Ketcham, R.A., 2015. Technical note: calculation of stoichiometry from EMP data for apatite and other phases with mixing monovalent anion sites. *Am. Min.* 100: 1620-1623.

- Kraml, M. Pik, R., Rahn, M., Selbekk, R., Carignan, J., Keller, J. 2006. A new multi-mineral age reference material for $^{40}\text{Ar}/^{39}\text{Ar}$, (U-Th)/He and fission track dating methods: The Limberg t3 tuff. *Geostandards and Geoanalytical Research*, 30: 73-86.
- Laslett, G.M., Gleadow, A., Duddy, I.R., 1994. The relationship between fission-track length and track density in apatite. *Nucl. Tracks* 9: 29-38.
- Leprêtre, R., Missenard, Y., Barbarand, J., Gautheron C., Saddiqi O., Pinna-Jamme R., 2015. Postrift history of the eastern central Atlantic passive margin: insights from the Saharan region of South Morocco. *J. Geophys. Res.* 120: 4645-4666.
- Menpes, R.J., 1997. Tertiary uplift and its implications for the tectonic evolution of sedimentary basins offshore South-West United Kingdom. PhD, The University of Adelaide (South Australia).
- McDowell, F.W., McIntosh, W.C., Farley, K.A., 2005. A precise ^{40}Ar - ^{39}Ar reference age for the Durango apatite (U-Th)/He and fission-track dating standard. *Chem. Geol.* 214: 249-263.
- Michard A., Saddiqi O., Chalouan A., De la Motte F., 2008. Continental evolution: the geology of Morocco. Structure, stratigraphy, and tectonics of the Africa-Atlantic Mediterranean triple junction. *Lecture Notes in Earth Sciences* 116, Springer Berlin.
- Miro S., Studer F., Constantini J.-M., Haussy J., Trouslard P., Grob J.-J., 2006. Effect of composition on helium diffusion in fluoroapatites investigated with nuclear reaction analysis. *J. Nucl. Mat.* 355, 1-9.
- Murray K.E., Orme D.A., Reiners P.W., 2014. Effects of U-Th-rich grain boundary phases on apatite Helium ages. *Chem. Geol.* 390, 135-151.
- Owen, T.R., 1976. The Geology of the Western Approaches. In Nairn, A.E.M. and Stehli, F.G (eds). *The ocean basins and margins, Vol.2: The North Atlantic*. Springer. 232-272.
- Peucat, J.J., 1986. Behaviour of Rb-Sr whole rock and U-Pb zircon systems during partial melting as shown in migmatitic gneisses from St Malo Massif, NE Brittany, France. *J. Geol. Soc* 143: 875-885.
- Pin, C., Peucat, J.J., 1986. Ages des episodes de metamorphisme paleozoïques dans le Massif central et le Massif armoricain. *Bull. Soc. Geol. France* 8: 461-469.
- Reiners, P.W., Farley, K.A., 2001. Influence of crystal size on apatite (U+Th)/He thermochronology: an example from the Bighorn Mountains, Wyoming. *Earth Planet. Sci. Lett.* 188, 413-420.
- Reiners, P.W., Brandon, M.T. 2005. Using thermochronology to understand orogenic erosion. *Annual Review of Earth and Planetary Sciences* 34: 419-466.
- Ruffel A., 1995. Evolution and hydrocarbon prospectivity of the Brittany Basin (Western Approaches Trough), offshore North-West France. *Marine Petrol. Geol.* 12: 387-407.
- Shuster, D., Flowers, R., Farley, K.A., 2006. The influence of natural radiation damage on helium diffusion kinetics in apatite. *Earth Planet. Sci. Lett.* 249: 148-161.
- Shuster D.L., Farley K.A., 2009. The influence of artificial radiation damage and thermal annealing on helium diffusion kinetics in apatite. *Geochim. Cosmochim. Acta.* 73: 183-196.
- Spiegel C., Kohn B., Belton D., Berner Z., Gleadow A., 2009. Apatite (U-Th-Sm)/He thermochronology of rapidly cooled samples: The effect of He implantation. *Earth Planet. Sci. Lett.* 285: 105-114.
- Stock G.M., Ehlers T.A., Farley K.A., 2006. Where does sediment come from? Quantifying catchment erosion with detrital apatite (U-Th)/He thermochronometry. *Geology* 34: 725-728.
- Siddall R., 1993. Thermotectonic evolution of the continental margins of the Bay of Biscay: application of apatite fission-track analysis. PhD, University of London.

- Valla, P.G., Shuster, D.L., Van der Beek P.A., 2011. Significant increase in relief of the European Alps during mid-Pleistocene glaciations. *Nature Geos.* 4: 688-692.
- Vermeesch P., Seward D., Latkoczy C., Wipf M., Günther D., Baur H., 2007. α -emitting mineral inclusions in apatite, their effect on (U-Th)/He ages, and how to reduce it. *Geochim. Cosmochim. Acta.* 71: 1737-1746.
- Vidal, P., Auvray, B., Charlot, R., Cogné, J., 1981. Precadomian relicts in the Armorican Massif: Their age and role in the evolution of the western and central European Cadomian-Hercynian belt. *Precambrian Res.* 14: 1-20.
- Wolf R., Farley K.A., Dass D., 1998. A sensitivity analysis of the apatite (U-Th)/He thermochronometer. *Chem. Geol.* 148, 105-114.
- Zeitler P.K. , Enkelmann E., Thomas J.B., Watson E.B., Ancuta L.D., Idleman B.D., 2017. Solubility and trapping of helium in apatite. *Geochimica et Cosmochimica Acta* 209: 1-8.
- Ziegler, P.-A., 1987. Evolution of the Western Approaches trough. *Tectonophysics*, 137: 341-346.

Table captions

Table 1: Sample lithology and location.

Table 2: AFT data.

Table 3: AHe age data and chemical composition for select elements.

Table 4: Apatite mean composition (wt%).

Figure captions

Figure 1: Geological setting and sample location. (A) Regional map of northwestern France, and location of the Armorican massif. Pink areas are outcropping Paleozoic basement massifs. (B) Geological map of the “pink granite coast” (Brittany, France), and location of the Ploumanac’h pluton. (C) Lithological map of the Ploumanac’h intrusion, and fission track analysis results (this study). Sample locations, crystallization ages, central AFT ages, and mean fission track lengths are shown.

Figure 2: Individual AHe dates as function of (A) effective U concentration and (B) alpha dose. The colors indicate sample location and lithology: PL10 (cyan squares), PL11 (dark purple diamonds), PL7 (light purple triangles), PL4 (yellow circles), PL6 (dark red circles), and external pink granites (red circles). Alpha dose was calculated from U, Th, and Sm contents over 250 Ma. In (B) only data where U, Th, and Sm were analyzed are shown.

Figure 3: Histograms of apatite chemical composition. Measurements were made on 339 single crystals, using EPMA. The dots represent the raw data, with the same color code than in Figure 3. Purple dots represent sample PL11. Units are oxide weights percent.

Figure 4: AHe dates as a function of (A) equivalent grain size and (B) crystal length. Pyr.: pyramidal termination. Bf.: Broken face. L: crystal length. Equivalent sphere radius size (R_s) was calculated based on measured individual grain dimensions.

Figure 5: Individual AHe dates as function of chemistry. Relationship between AHe date and Sr (A), Ba (B), and La concentrations (D). Relationship between eU and Sr content (C). Error bars represent maximum uncertainties, i.e. 8% for AHe, 15% for Sr and La and eU, and 10 % for Ba. The color coding is the same as for Fig. 1, 3, and 4.

Figure 6: Thermal history reconstruction and forward simulations. (A) Thermal history reconstruction resulting from inverse simulation of the AFT dataset, along with geological constraints, using QTQt (Gallagher, 2012). (B) Forward simulations of AFT dataset using this (T-t) path (green squares) or a 80°C Jurassic reheating (red squares) using QTQt. The yellow square is issued from the inversion of PL1 only. (C) Forward simulation performed using the Flowers et al. (2009) model, with two different burial temperature, carried out with QTQt. (D) Forward simulations using the Gautheron et al. (2009) model, carried out using QTQt for two different burial temperatures. The error bar on raw AHe ages is 5%.

Figure 7: Evolution of the AHe dates as a function of the trapping energy. Forward simulations of AHe dates using Gerin et al. (2017), with constant damage annealing rate ($rmro'=rmro$). (A) Forward simulation results of the AHe vs eU relationship obtained for $\Delta Ea=30$ kJ/mol (red triangles), 40 kJ/mol (yellow losangles), and $\Delta Ea=70$ kJ/mol (green squares), compared to observations (blue dots). (C) and (D): ΔEa calibration obtained for sample PL10 and PL4. Colors and numbers indicate ΔEa values (see color code). Squares represent AFT data and triangles represent AHe dates.

Figure 8: Evolution of the inferred trapping energy ΔEa with the effective uranium (eU). Results for PL4 and PL10, which required trapping energy range from 46 to 120 kJ/mol.

Figure 9: Damage annealing simulation. Forward simulations of AHe dates were performed using Gerin et al. (2017), using the thermal history obtained from geological and AFT constraints. Alpha damage annealing rate is quantified by a variable rmr_0' . (A) AHe vs eU relationship obtained for $\text{rmr}_0'=0.7$ (red triangles) and 0.9 (green squares) with $\Delta Ea=70$ kJ/mol and (B) $\Delta Ea=40$ kJ/mol.

Figure 1

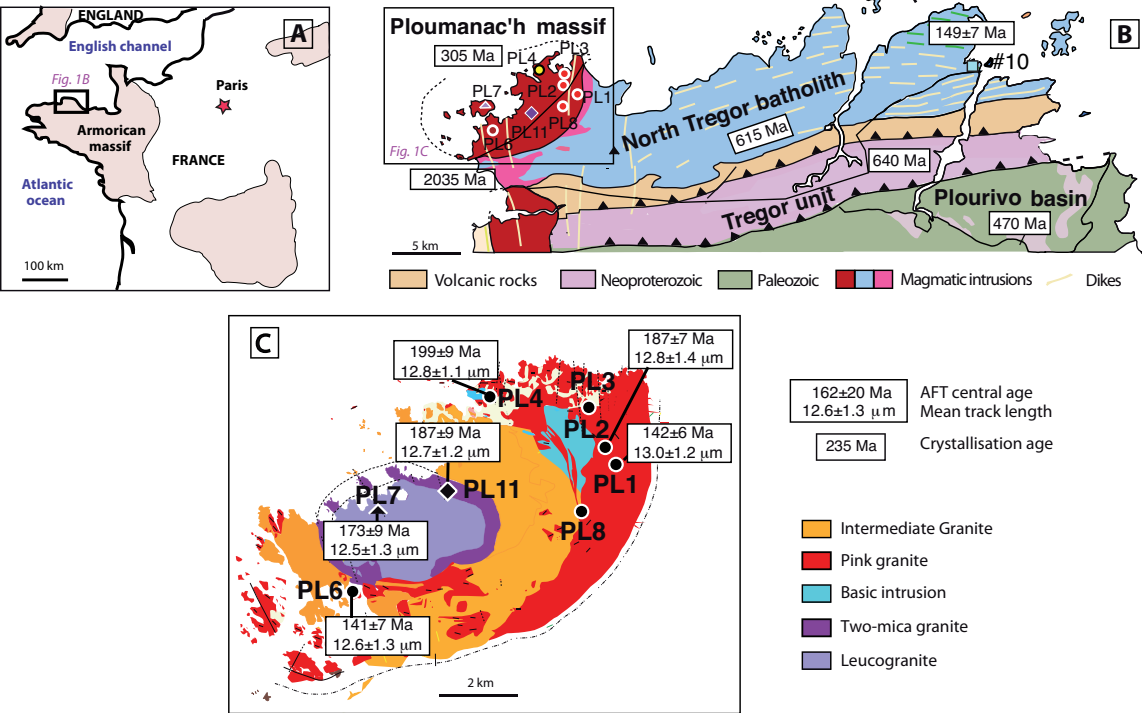


Figure 2

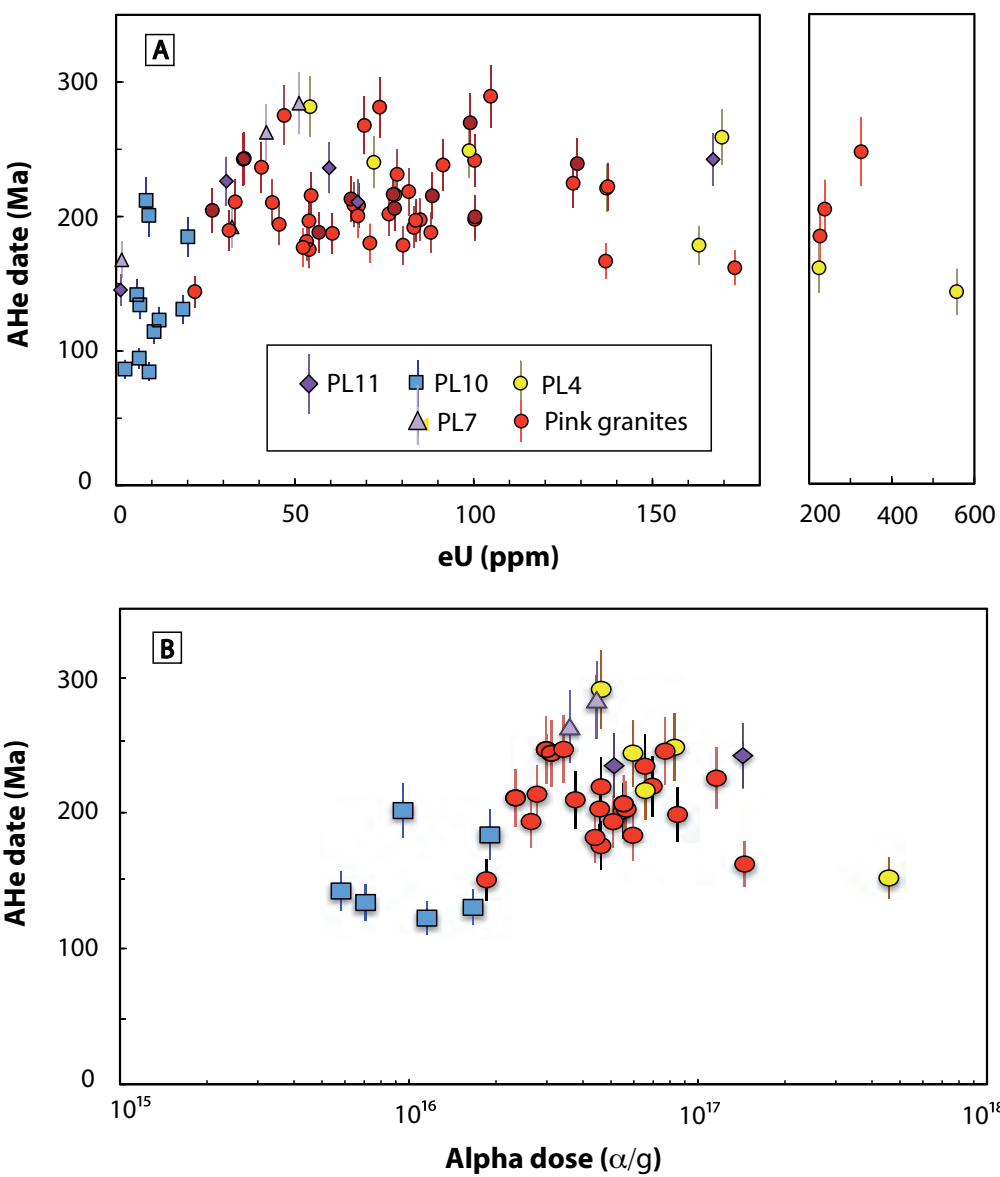


Figure 3

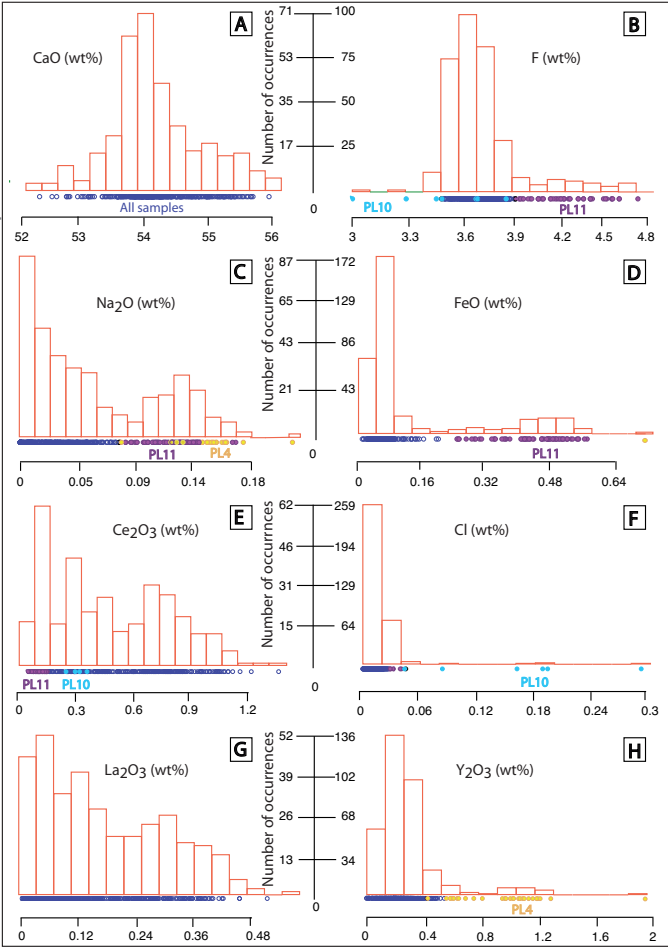


Figure 4

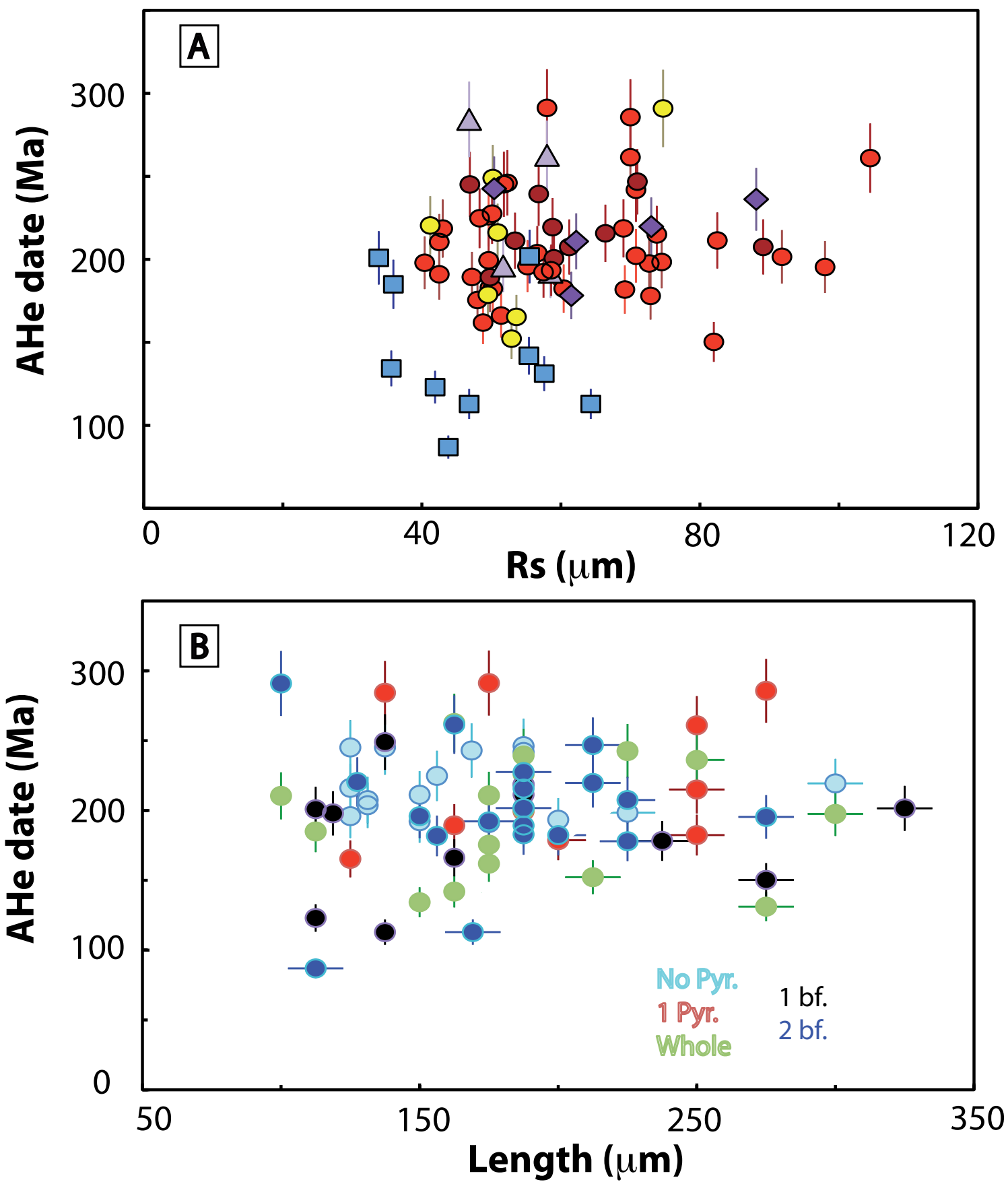


Figure 5

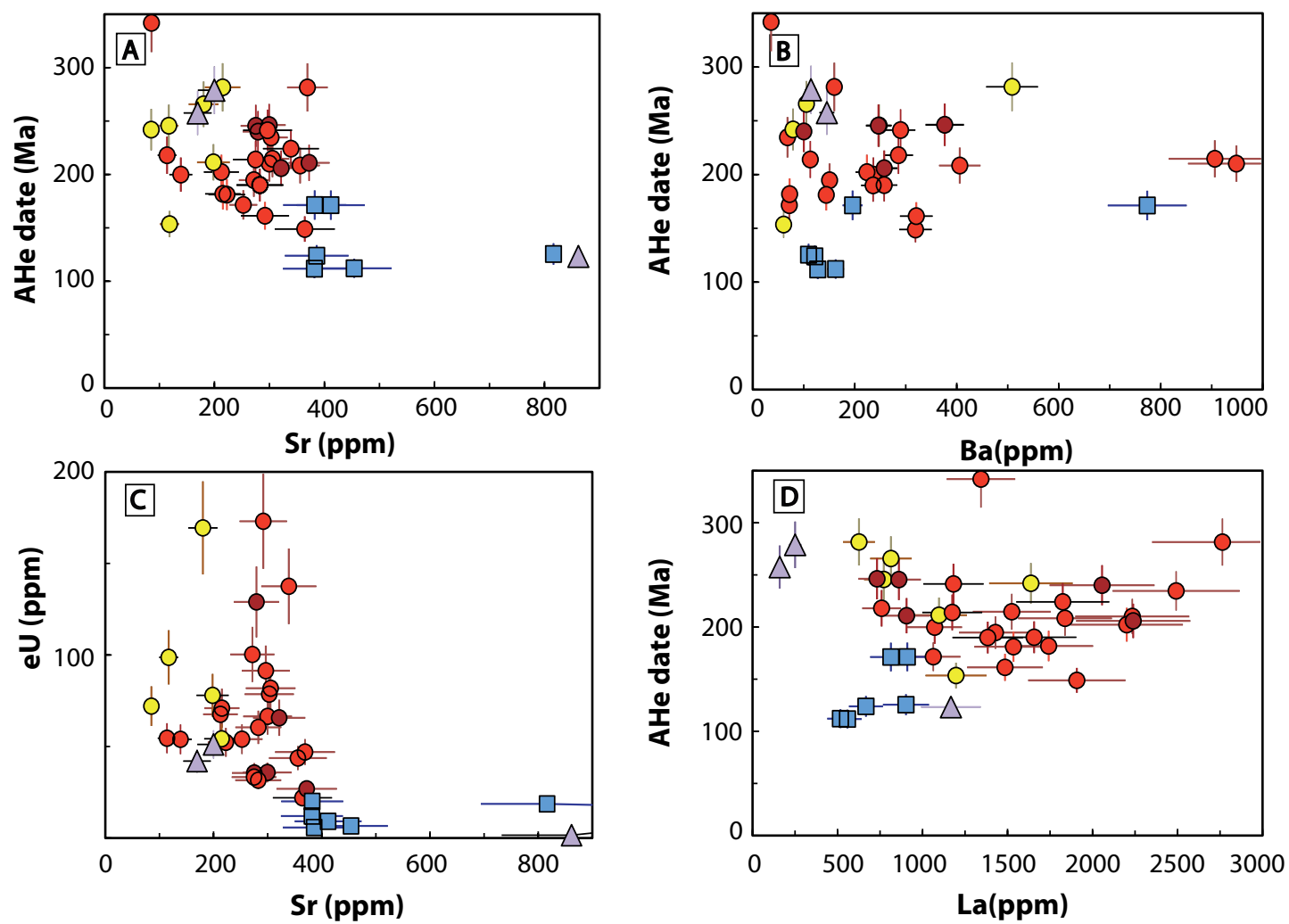


Figure 6

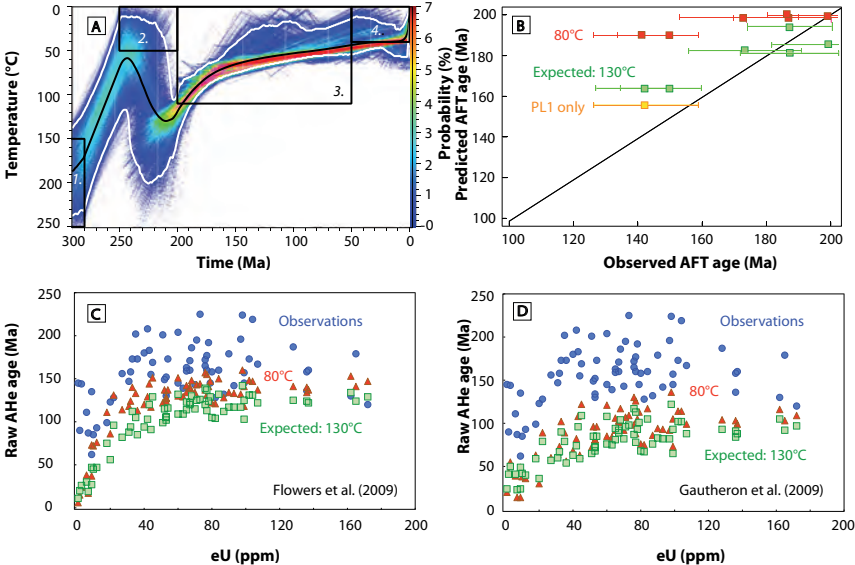


Figure 7

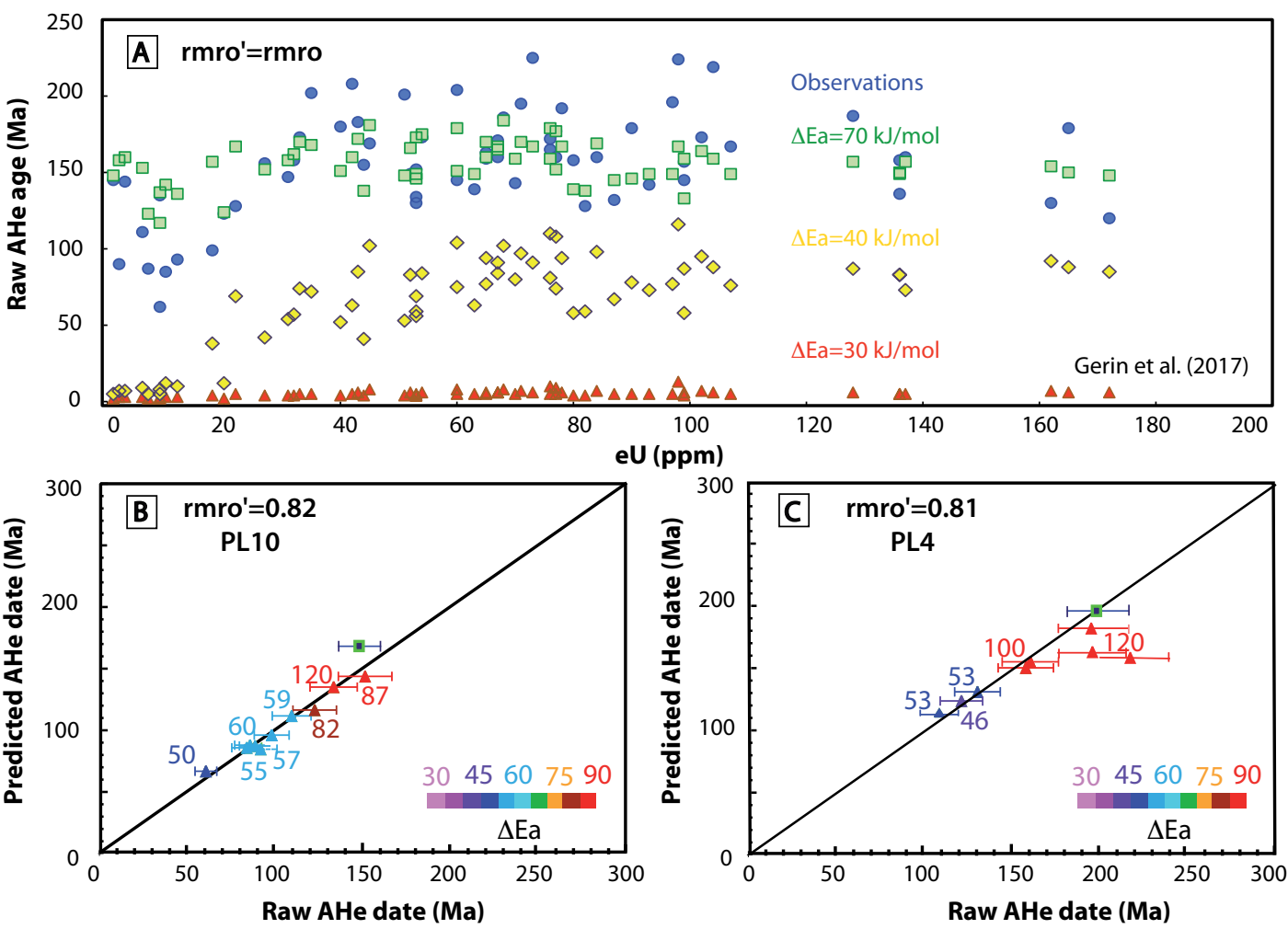


Figure 8

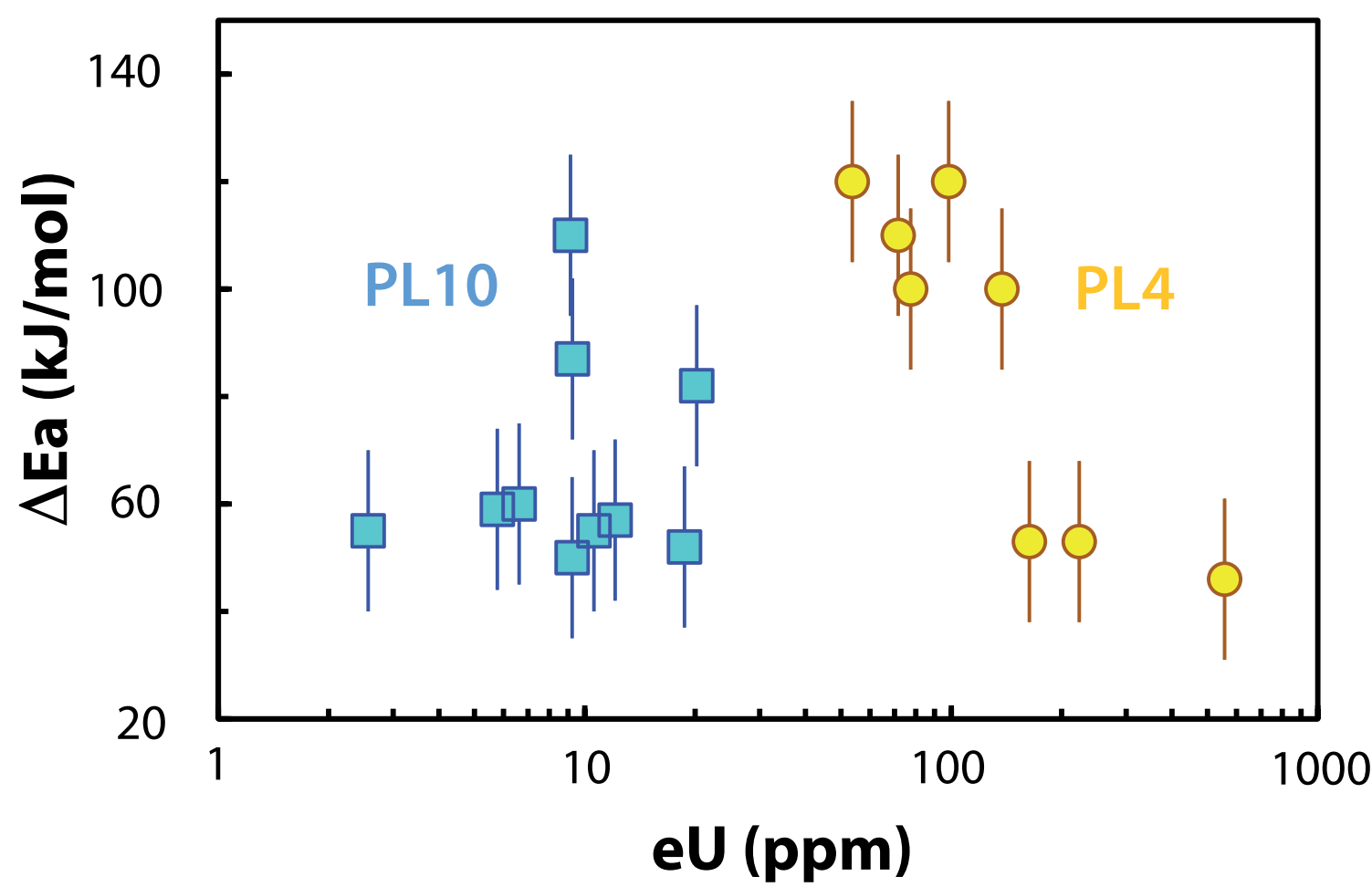


Figure 9

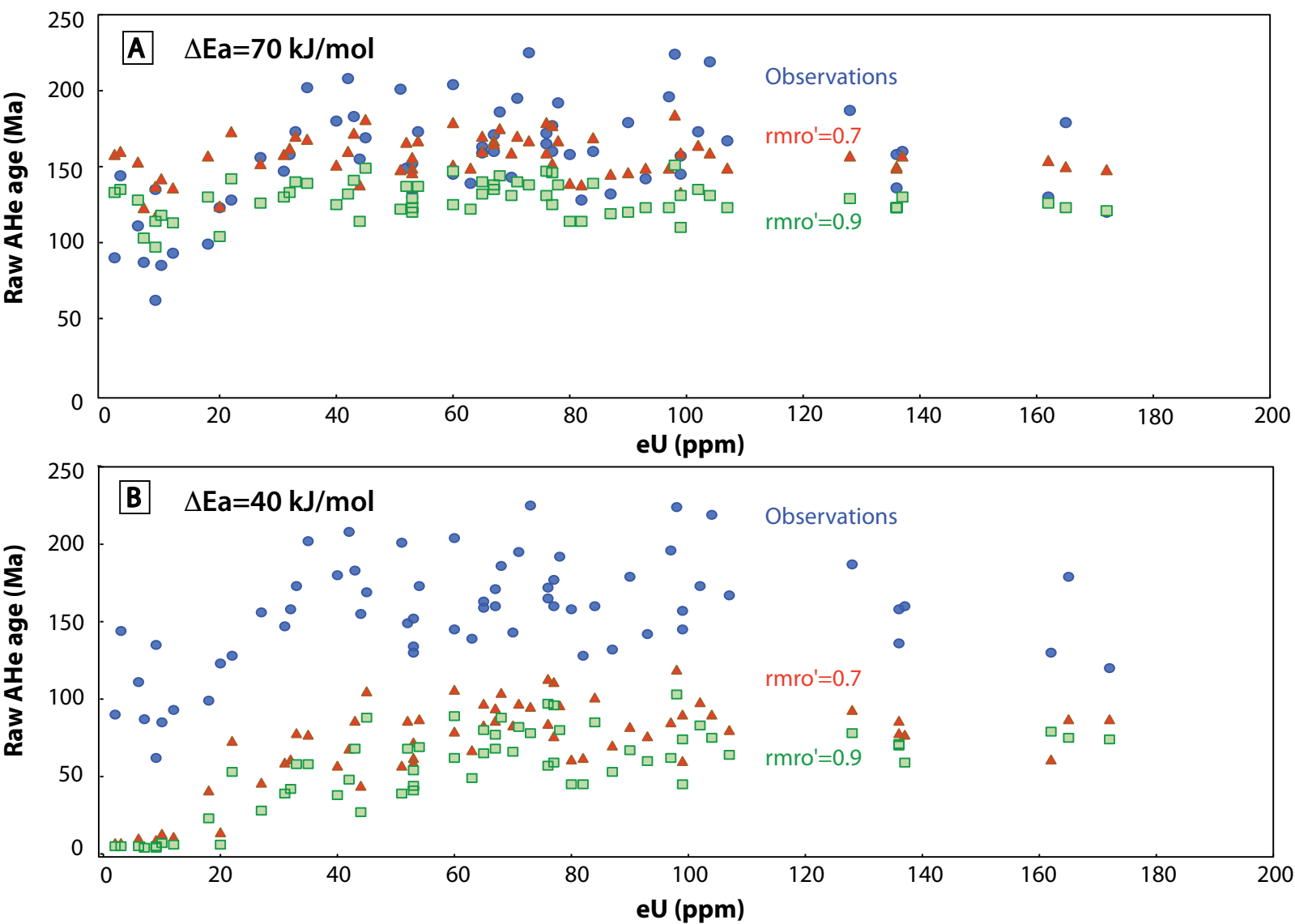


Table 1: Sample petrology and location.

<i>Samples</i>	<i>Petrography</i>	<i>Altitude (m)</i>	<i>Coordinates</i>
Ploumanac’h extern layer			
PL 1	Coarse-grained syenogranite	34	N48°48'54,4-W003°28'37,3
PL 2	Coarse-grained syenogranite	16	N48°49'11,6-W003°29'32,6
PL 3	Coarse-grained monzogranite	0	N48°49'47,9-W003°29'38,6
PL 4	Medium-grained granitoid	0	N48°49'52,7-W003°31'22,4
PL 6	Coarse-grained monzogranite	21	N48°47'09,7-W003°34'32,0
PL 8	Coarse-grained monzogranite	50	N48°48'19,9-W003°29'32,7
Ploumanac’h inter layer			
PL 7	Mono-mica leucogranite	28	N48°48'19,2-W003°34'18,8
PL 11	Two mica granite	3	N48°48'34,4-W003°32'50,1
Trégor			
PL 10	Granodiorite	0	N48°51'10,8-W003°12'39,3

Table 2: AFT data.

Sample name	No. of grains	No. of tracks	$\rho_s \times 10^6$ (tr/cm ²)	N _s	$\rho_i \times 10^6$ (tr/cm ²)	N _i	$\rho_d \times 10^5$ (tr/cm ²)	N _d	P(χ^2) (%)	AFT $\pm \sigma$ (Ma)	D (%)	MTL \pm SD (μ m)	Dpar \pm SD (μ m)
PL 1	20	100	3.234	1504	2.742	1275	7	7671	63	142 \pm 6	0.9	13.0 \pm 1.2	1.3 \pm 0.1
PL 2	23	102	3.849	2321	2.463	1485	7	7671	60	187 \pm 7	1.4	12.8 \pm 1.4	1.5 \pm 0.1
PL 4	24	100	2.912	1491	1.750	896	7	7671	49	199 \pm 9	1.8	12.8 \pm 1.1	1.4 \pm 0.1
PL 6	20	100	2.728	1506	1.893	1045	5.5	6040	54	141 \pm 7	2.5	12.6 \pm 1.3	1.9 \pm 0.1
PL 7	23	78	2.593	1006	1.794	696	7	7671	85	173 \pm 9	0.0	12.5 \pm 1.3	1.4 \pm 0.1
PL 10	23	NA*	3.764	1566	3.024	1258	7	7671	46	149 \pm 7	2.8	NA	1.5 \pm 0.5
PL 11	20	95	3.145	1557	2.008	994	7	7671	68	187 \pm 9	1.2	12.7 \pm 1.2	1.4 \pm 0.1

* NA=analysed

No. of grains and No. of tracks mean number of counted grains and number of measured tracks lengths

Table 3: AHe age data and selected chemical contents.

<i>Name</i>	<i>Geometry</i>	<i>L</i> (μm)	<i>H</i> (μm)	<i>W</i> (μm)	<i>Rs</i> (μm)	<i>F_T</i>	<i>Masse</i> (μg)	<i>⁴He</i> ($\times 10^5$) (ncc/g)	<i>U</i> (ppm)	<i>Th</i> (ppm)	<i>Sm</i> (ppm)	<i>eU</i> (ppm)	<i>Th/U</i>	<i>Age</i> <i>raw</i> (Ma)	<i>Age c</i> (Ma) *	<i>Mn</i> (ppm)	<i>Sr</i> (ppm)	<i>Ba</i> (ppm)	ΣREE (ppm)
<i>PL1F</i>	<i>1 py</i>	175	175	113	58	0.75	4.7	28.21	66	162	352	105	2.5	219	291 \pm 23	-	-	-	-
<i>PL1D</i>	<i>1 py</i>	250	238	238	105	0.86	22.5	19.17	46	99	254	69	2.2	224	261 \pm 21	-	-	-	-
<i>PL1G</i>	<i>2bf</i>	188	175	163	83	0.88	12.5	15.53	39	122	236	68	3.2	186	211 \pm 17	-	-	-	-
PL1terB	No py	188	125	119	69	0.79	8.9	11.55	33	91	129	55	2.8	173	219 \pm 18	702	114	286	9025
PL1bisA	2bf	275	125	150	82	0.85	16.5	3.43	11	46	58	22	4.2	128	150 \pm 12	449	364	319	12307
PL1QuA	No py	131	113	100	57	0.75	4.7	9.96	25	120	204	54	4.8	152	204 \pm 16	752	139	237	11428
PL 2																			
PL2-B	1+1	100	100	88	43	0.74	3.2	8.32	22	92	183	44	4.3	155	210 \pm 17	449	356	406	11791
PL2-C	1+1	175	88	88	48	0.74	2.6	8.51	28	108	235	54	3.9	130	176 \pm 14	353	253	72	7145
PL2-D	2bf	188	75	75	43	0.72	2.4	15.69	43	161	306	82	3.7	158	219 \pm 18	739	306	906	9872
PL2-E	2bf	119	81	69	40	0.73	1.6	17.61	53	196	354	100	3.7	145	198 \pm 16	412	272	151	9900
<i>PL2A</i>	<i>No py</i>	175	75	75	43	0.67	2.2	12.93	43	168	270	83	3.9	127	191 \pm 15	-	-	-	-
<i>PL2B</i>	<i>1bf</i>	225	138	138	73	0.82	9.7	14.23	39	172	270	80	4.4	145	178 \pm 14	-	-	-	-
<i>PL2C</i>	<i>1+1</i>	300	150	125	73	0.81	10.2	16.61	42	179	311	85	4.3	160	198 \pm 16	-	-	-	-
<i>PL2D</i>	<i>1bf</i>	188	100	88	50	0.73	3.5	8.78	28	107	301	53	3.9	134	183 \pm 15	-	-	-	-
<i>PL2E</i>	<i>1py</i>	163	88	88	47	0.70	2.4	14.09	46	175	270	88	3.8	132	189 \pm 15	-	-	-	-
<i>PL2F</i>	<i>1bf</i>	275	200	188	98	0.87	22.8	9.38	24	89	285	46	3.7	169	195 \pm 16	-	-	-	-
<i>PL2G</i>	<i>2bf</i>	325	200	163	92	0.85	21.8	16.04	38	160	321	76	4.2	172	202 \pm 16	-	-	-	-
PL2bisB	No py	225	138	119	75	0.81	11.8	13.66	34	134	97	66	3.9	163	202 \pm 16	452	303	68	16070
PL2bisC	1bf	163	138	125	70	0.82	8.9	18.41	40	161	129	79	4.0	192	234 \pm 19	855	86	36	12731
PL3																			
PL3-B	1+1	175	125	88	49	0.74	3.0	25.30	87	360	353	173	4.2	120	162 \pm 13	701	292	321	11534
<i>PL3A</i>	<i>1+1</i>	188	100	88	50	0.73	3.0	65.69	152	726	1223	326	4.8	165	226 \pm 18	-	-	-	-
<i>PL3B</i>	<i>2bf</i>	163	88	88	51	0.82	3.4	22.75	64	305	306	137	4.8	136	166 \pm 13	-	-	-	-
<i>PL3C</i>	<i>1bf</i>	150	100	100	55	0.78	3.9	44.15	106	548	633	238	5.2	153	196 \pm 16	-	-	-	-
<i>PL3D</i>	<i>1pyr</i>	250	125	113	50	0.72	4.2	35.80	109	489	513	226	4.5	130	182 \pm 15	-	-	-	-
PL3bisA	No py	188	144	113	71	0.79	9.7	13.18	29	162	118	68	5.6	160	202 \pm 16	479	213	224	16625
PL3bisB	1bf	200	119	88	60	0.78	6.7	12.33	35	150	162	71	4.3	143	182 \pm 16	496	215	72	13215
PL3bisC	1bf	156	138	125	69	0.82	8.6	9.49	27	106	125	52	3.9	149	182 \pm 15	529	223	144	12074
PL4																			
PL4-E	2py	213	113	100	59	0.79	3.9	81.36	240	1320	291	557	5.5	120	152 \pm 12	719	118	61	13837
PL4-H	np	125	113	100	53	0.74	3.4	15.08	35	177	285	78	5.0	160	216 \pm 17	884	198-	3217-	38140-
PL4-I	2bf	138	100	100	51	0.79	3.1	23.53	41	239	334	99	5.8	196	249 \pm 20	817	117	248	39516
<i>PL4B</i>	<i>1bf</i>	128	125	100	50	0.72	4.2	26.35	76	256	480	137	3.4	158	220 \pm 18	-	-	-	-
<i>PL4D</i>	<i>1py</i>	125	88	88	41	0.66	1.5	29.34	107	485	400	224	4.5	108	165 \pm 13	-	-	-	-

<i>PL4E</i>	<i>lpy</i>	200	125	113	54	0.73	3.9	25.76	81	343	487	163	4.3	130	179±14				
PL4bisC	No py	169	163	125	75	0.80	11.0	17.01	33	161	114	72	4.8	195	243±19	893	85	79	16307
PL6																			
PL6-C	1+1	188	113	94	57	0.78	4.0	29.43	65	268	245	129	4.1	187	239±19	601	279	100	14173
<i>PL6A</i>	<i>lbf</i>	188	100	88	50	0.73	3.5	10.65	33	127	167	57	3.9	139	189±15	-	-	-	-
<i>PL6B</i>	<i>No py</i>	300	100	100	59	0.75	6.8	15.46	43	142	150	77	3.3	165	219±18	-	-	-	-
<i>PL6D</i>	<i>lbf</i>	188	150	125	66	0.80	7.4	21.68	50	221	174	88	4.4	173	216±17	-	-	-	-
<i>PL6E</i>	<i>lbf</i>	225	200	175	89	0.85	16.9	16.81	40	158	150	78	4.0	177	207±17	-	-	-	-
<i>PL6F</i>	<i>1+1</i>	188	113	113	59	0.78	4.4	18.99	52	199	150	100	3.8	157	201±16	-	-	-	-
PL6bisA	lbf	213	125	119	71	0.82	10.1	8.77	22	56	81	36	2.6	202	247±20	443	275	247	5388
PL6bisB	No py	125	94	75	47	0.71	2.8	7.72	23	56	128	36	2.5	173	245±20	436	299	376	4554
PL6bisC	No py	131	125	113	61	0.77	5.9	12.66	32	141	162	66	4.5	159	207±18	1017	321	258	15340
PL6bisD	No py	150	100	88	53	0.74	4.2	5.20	17	43	106	27	2.6	156	211±17	481	372	2817	5878
PL7																			
PL7-AA	1+1	163	125	100	58	0.79	3.9	10.68	39	11	155	42	0.3	208	263±21	2243	170	145	2047
PL7-BB	lpy	138	94	88	47	0.71	2.1	12.66	48	13	241	51	0.3	201	284±23	3112	200	114	2912
<i>PL7A</i>	<i>No py</i>	125	100	100	52	0.74	3.1	0.29	1.3	0.6	139	2	0.5	145	196±16	-	-	-	-
<i>PL7B</i>	<i>lbf</i>	175	125	88	59	0.82	4.9	6.27	32.3	1.2	151	32	0.0	158	192±15	-	-	-	-
PL8																			
<i>PL8C</i>	<i>lbf</i>	188	113	88	50	0.73	3.7	22.05	56	218	212	128	3.9	167	228±18	-	-	-	-
<i>PL8D</i>	<i>lpyr</i>	275	125	125	70	0.79	8.4	20.36	38	150	250	74	4.0	225	286±23	-	-	-	-
<i>PL8E</i>	<i>lpyr</i>	188	100	88	50	0.71	3.0	16.09	51	177	277	84	3.5	142	199±16	-	-	-	-
PL8bisA	No py	200	88	88	59	0.76	10.4	5.60	16	64	89	32	3.9	147	193±15	590	283	258	12756
PL8bisB	lpyr	250	150	150	74	0.81	19.7	7.00	19	59	57	33	3.1	173	215±17	588	275	113	8439
PL8bisD	No py	188	100	75	52	0.73	4.5	8.84	22	76	152	41	3.4	180	246±20	-	-	-	-
PL8bisE	No py	138	113	100	52	0.73	3.3	19.79	48	180	262	91	3.7	179	245±20	492	297	290	9097
PL8bisC	No py	156	106	88	48	0.71	3.0	26.82	70	283	331	138	4.1	160	225±18	579	339	2822	13704
PL8terA	No py	150	125	88	58	0.75	5.3	10.62	31	122	176	60	3.9	145	192±15	6278	283	236	13040
PL 10																			
PL10-A	1+1	113	69	69	36	0.67	1.0	3.09	12.8	30.3	306	20	2.4	123	185±15	959	382	196	5909
PL10-B	2bf	113	100	88	42	0.76	1.7	1.39	7.3	19.6	203	12	2.7	93	123±10	645	382	128	3430
PL10-D	2bf	113	63	63	34	0.67	1.0	1.54	4.7	18.5	250	9	3.9	135	201±16	1709	412	774	5233
PL10-F	1+1	150	63	63	36	0.65	1.2	0.72	4.1	10.5	199	7	2.6	87	134±11	681	454	163	3093
PL10-I	2py	275	100	94	58	0.76	4.7	2.27	10.5	34.2	157	19	3.3	99	131±10	692	816	109	5163
PL10-L	1+1	163	113	100	55	0.78	3.5	0.80	3.9	7.8	129	6	2.0	111	142±11	740	386	122	4053
<i>PL10A</i>	<i>lbf</i>	169	138	125	64	0.80	6.4	0.29	1.1	6.1	104	2	5.6	90	113±9	-	-	-	-
<i>PL10B</i>	<i>2bf</i>	138	100	88	47	0.75	2.6	1.10	5.0	23.3	100	11	4.6	85	113±9	-	-	-	-
<i>PL10G</i>	<i>lbf</i>	113	88	88	44	0.71	2.0	0.70	4.1	21.4	100	9	5.3	62	87±7	-	-	-	-
PL 11																			
PL11-C	1+1	225	88	88	50	0.74	3.5	36.36	100	278	707	167	2.8	179	243±19	-	-	-	-

PL11E	1+1	250	181	175	88	0.87	14.0	15.06	57.7	7.8	185	60	0.1	204	236±19	-	-	-	-
<i>PL11A</i>	<i>2bf</i>	238	188	113	62	<i>0.81</i>	8.3	<i>0.49</i>	<i>1.9</i>	2.5	239	<i>1</i>	<i>1.3</i>	<i>144</i>	<i>178±14</i>	-	-	-	-
<i>PL11B</i>	<i>1 bf</i>	213	200	138	73	<i>0.83</i>	<i>10.9</i>	<i>9.98</i>	<i>42.5</i>	5.2	207	<i>31</i>	<i>0.1</i>	<i>183</i>	<i>220±18</i>	-	-	-	-
PL11-A	1+1	175	125	125	62	0.81	4.9	14.17	67.1	1.9	150	68	0.0	171	211±17	-	-	-	-

* are alpha ejection corrected age.

Italic samples and results refer to data were a mean value of Sm content as been used in the AHe age calculation.

ΣREE is the sum of analyzed rare earth elements: La, Ce, Pr, Nd, Sm, Eu, Gd, Tb, Ho, Er, Tm, Yb and Lu.

Table 4: Apatite mean composition (wt%).

<i>Sample name</i>	<i>P₂O₅</i>	<i>CaO</i>	<i>F</i>	<i>Cl</i>	<i>SO₃</i>	<i>SiO₂</i>	<i>FeO</i>	<i>MgO</i>	<i>MnO</i>	<i>Na₂O</i>	<i>Y₂O₃</i>	<i>La₂O₃</i>	<i>Ce₂O₃</i>	<i>Sm₂O₃</i>	<i>SrO</i>	<i>Pr₂O₃</i>	<i>Nd₂O₃</i>	<i>(OH)</i>	<i>Total</i>
PL 1	40.59	54.16	3.75	0.01	0.02	0.56	0.06	0.01	0.09	0.04	0.39	0.14	0.45	0.01	0.00	0.08	0.36	0.00	100.7
	±0.45	±0.36	±0.25	±0.01	±0.03	±0.15	±0.04	±0.01	±0.02	±0.03	±0.09	±0.07	±0.18	±0.01	±0.01	±0.05	±0.13	±0.00	
PL 2	40.90	54.09	3.63	0.02	0.01	0.64	0.06	0.01	0.04	0.03	0.18	0.29	0.77	0.01	0.01	0.10	0.43	0.00	101.2
	±0.51	±0.47	±0.11	±0.00	±0.01	±0.22	±0.02	±0.01	±0.02	±0.03	±0.06	±0.11	±0.25	±0.01	±0.02	±0.05	±0.14	±0.00	
PL 3	41.17	54.13	3.68	0.02	0.02	0.66	0.07	0.01	0.05	0.03	0.23	0.24	0.69	0.01	0.01	0.11	0.44	0.00	101.6
	±0.49	±0.50	±0.13	±0.01	±0.05	±0.24	±0.04	±0.01	±0.01	±0.02	±0.09	±0.10	±0.26	±0.01	±0.02	±0.06	±0.15	±0.00	
PL 4	40.52	53.31	3.81	0.01	0.04	0.67	0.09	0.00	0.10	0.13	0.93	0.11	0.41	0.01	0.00	0.07	0.40	0.04	100.7
	±0.68	±0.52	±0.16	±0.01	±0.14	±0.29	±0.13	±0.01	±0.02	±0.03	±0.32	±0.06	±0.19	±0.01	±0.01	±0.05	±0.13	±0.13	
PL 6	40.41	54.11	3.59	0.01	0.02	0.53	0.10	0.01	0.05	0.01	0.16	0.20	0.53	0.01	0.02	0.07	0.31	0.00	101.5
	±0.69	±0.60	±0.15	±0.01	±0.05	±0.29	±0.04	±0.01	±0.01	±0.01	±0.09	±0.10	±0.28	±0.02	±0.04	±0.05	±0.17	±0.00	
PL 8	42.51	54.90	3.66	0.02	0.01	0.52	0.06	0.01	0.06	0.01	0.18	0.16	0.48	0.01	0.03	0.07	0.31	0.00	103.0
	±0.68	±0.51	±0.17	±0.00	±0.01	±0.28	±0.02	±0.01	±0.02	±0.01	±0.10	±0.09	±0.25	±0.01	±0.04	±0.05	±0.16	±0.00	
PL 10	41.45	54.59	3.45	0.16	0.01	0.17	0.14	0.02	0.12	0.06	0.09	0.12	0.29	0.00	0.09	0.03	0.15	0.00	100.9
	±0.39	±0.07	±0.29	±0.09	±0.01	±0.04	±0.04	±0.01	±0.03	±0.02	±0.02	±0.02	±0.04	±0.00	±0.02	±0.05	±0.03	±0.00	
PL 11	41.42	54.06	3.90	0.01	0.01	0.01	0.42	0.07	0.52	0.12	0.25	0.04	0.11	0.00	0.10	0.02	0.08	0.00	101.1
	±0.37	±0.27	±0.26	±0.01	±0.01	±0.02	±0.12	±0.02	±0.10	±0.02	±0.05	±0.03	±0.03	±0.01	±0.02	±0.03	±0.03	±0.00	

Here the mean and standard deviation of individual grain composition are presented. EMP analyses were carried out on 50 grains per sample.

Background dataset for online publication only

[Click here to download Background dataset for online publication only: Recanati-DataRep-Revision.docx](#)